processes

MDPI

Article

Design of Intelligent Nonlinear H_2/H_∞ Robust Control Strategy of Diesel Generator-Based CPSOGSA Optimization Algorithm

Yidong Zou [1,†], Boyi Xiao [2,†], Jing Qian [2] and Zhihuai Xiao [1,*]

[1] School of Power and Mechanical Engineering, Wuhan University, Wuhan 430072, China; yidongzou@whu.edu.cn
[2] Faulty of Metallurgical and Energy Engineering, Kunming University of Science and Technology, Kunming 650000, China
* Correspondence: xiaozhihuai@126.com
† These authors contributed equally to this work.

Abstract: In today's human society, diesel generators (DGs) are widely applied in the human energy and electricity supply system due to its technical, operational, and economic advantages. This paper proposes an intelligent nonlinear H_2/H_∞ robust controller based on the chaos particle swarm gravity search optimization algorithm (CPSOGSA), which controls the speed and excitation of a DG. In this method, firstly, establish the nonlinear mathematical model of the DG, and then design the nonlinear H_2/H_∞ robust controller based on this. The direct feedback linearization and the H_2/H_∞ robust control theory are combined and applied. Based on the design of the integrated controller for DG speed and excitation, the system's performance requirements are transformed into a standard robust H_2/H_∞ control problem. The parameters of the proposed solution controller are optimized by using the proposed CPSOGSA. The introduction of CPSOGSA completes the design of an intelligent nonlinear H_2/H_∞ robust controller for DG. The simulation is implemented in MATLAB/Simulink, and the results are compared with the PID control method. The obtained results prove that the proposed method can effectively improve the dynamic accuracy of the system and the ability to suppress disturbances and improve the stability of the system.

Keywords: diesel generator; speed and excitation control; robust control; intelligent optimization

Citation: Zou, Y.; Xiao, B.; Qian, J.; Xiao, Z. Design of Intelligent Nonlinear H_2/H_∞ Robust Control Strategy of Diesel Generator-Based CPSOGSA Optimization Algorithm. *Processes* **2023**, *11*, 1867. https://doi.org/10.3390/pr11071867

Academic Editor: Hsin-Jang Shieh

Received: 25 May 2023
Revised: 12 June 2023
Accepted: 16 June 2023
Published: 21 June 2023

1. Introduction

The diesel generator (DG) is a prominent energy and power equipment extensively employed within the human industrial system [1]. Its versatility is especially crucial in regions characterized by weak grids and high costs associated with long-distance power transmission. Furthermore, in specific power supply scenarios such as military emergency power supply and disaster relief power supply, the reliance on traditional large power grids for providing adequate and timely power becomes impractical [2–4]. The wide range of applications of diesel generators is shown in Figure 1. In such contexts, DGs and their associated systems prove to be highly effective and reliable alternatives. However, to ensure the optimal performance and operational stability of DG systems, it is essential to develop advanced control strategies that can effectively regulate and optimize their operation.

The system consisting of DGs and the various types of loads connected can be considered a micro-grid (MG) [5]. The MG is an effective way to accelerate renewable energy development and solve the shortcomings of large grids [6]. The complementation of photovoltaic panels, wind turbines, and DGs in MG is one of the development trends of power generation and distribution in the future power system [7]. With the continuous improvement and perfection of DG technology, more and more people will also benefit from it, especially far away from the large grid. Therefore, the DG research work has progressive significance for the energy supply of human society.

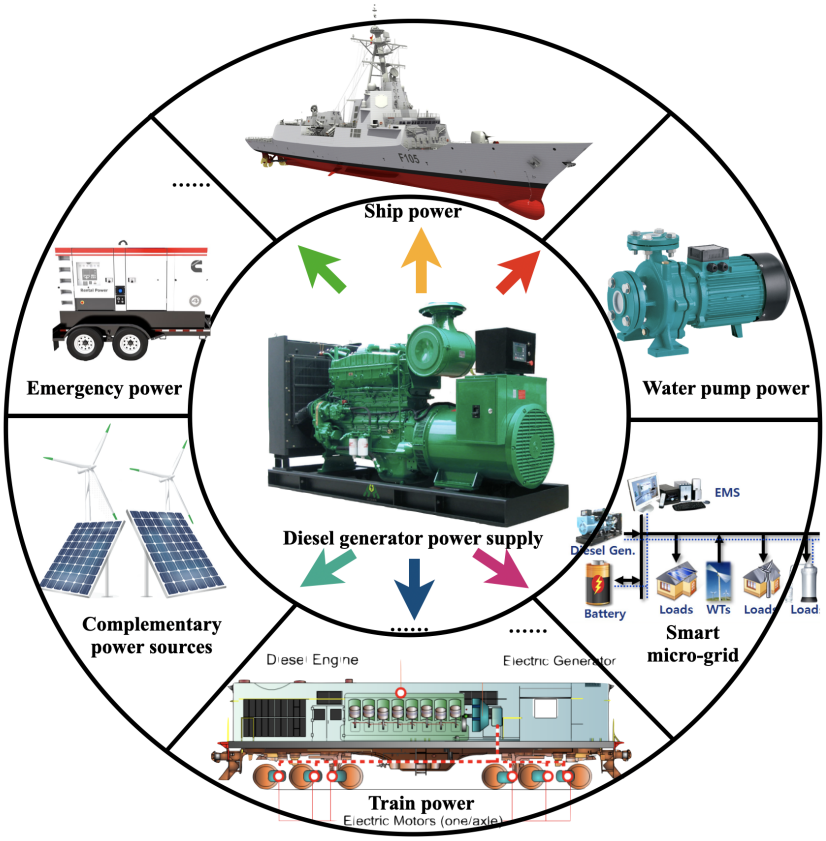

Figure 1. Widely used energy power device—diesel generator.

In many MGs, the DG is typically configured as the primary power source to ensure the safe and stable operation of the MG system [8,9]. Considering that DGs often contribute significantly to the overall capacity of most MGs, their control performance plays a critical role in determining the stability of the entire MG [10]. As a result, research focused on DG control is of fundamental importance. However, based on the current state of research, the comprehensive disturbance characteristics, such as voltage and frequency, specific to distributed MGs are rarely considered in the conventional DG control studies [11,12]. To address this gap, it is crucial to develop advanced control strategies that account for the intricate dynamics and disturbance characteristics associated with distributed MGs. By considering factors such as fluctuating loads, intermittent renewable energy sources, and varying grid conditions, the control of DGs can be significantly improved to ensure the optimal performance, stability, and resilience of the entire MG system.

The speed control system, comprising the diesel engine (DE) and the governor, plays a crucial role in determining the frequency of the synchronous generator. The frequency stability of the MG system relies heavily on the characteristics of the DE governor system [13,14]. However, when there are sudden changes in the load within the MG system, the power flow and output power of each generator also experience abrupt variations, disrupting the power balance between the generator and the prime mover. This leads to the occurrence of unbalanced torque and relative motion between the rotors of the generators [15]. The resulting frequency fluctuations not only impact the system's users but also detrimentally affect the overall operation of the MG system. Consequently, it becomes necessary to adjust the prime mover's frequency [16,17]. While much of the existing research has focused on optimizing the speed controller, there are limitations to the conventional approaches. For instance, Valenzuela et al. [18] proposed a conventional PI speed controller with reduced bandwidth to suppress excitation at the resonant frequency, but this approach leads to slow dynamic performance, which is undesirable. Mahmoud et al. [19] analyzed optimal tuning methods for the PI/PID controller to enhance system performance. However,

this technique proves ineffective when the inertia of the driving machine is comparable to that of the load device [20]. In addition to these conventional approaches, advanced control strategies, such as sliding mode controller [21], model predictive control [22], fuzzy logic [23], neural networks [24,25], and optimization algorithms [26], have been proposed for speed controller optimization. These solutions exhibit improved dynamic properties and robustness against parameter changes. However, these works have not adequately considered the effects of the excitation regulation process. Moreover, in extreme cases, these methods may not be applicable to DG systems. In light of these limitations, it is essential to explore alternative control strategies that address the challenges associated with speed control in DG systems.

The balance between the mechanical power of the prime mover and the electromagnetic power of the generator is crucial to ensure stable operation. Failure to achieve this balance can result in rotor oscillations, electromagnetic transient processes, and dynamic excitation regulation caused by voltage and current fluctuations at the generator terminal [27,28]. Since the majority of electrical equipment in DG systems comprises inductive loads, the load current has a demagnetizing effect on the synchronous generator. Changes in current magnitude and power factor directly impact the terminal voltage, necessitating the use of an excitation control device for the synchronous generator [29]. Furthermore, to enhance power supply reliability and achieve cost-effective electricity generation, the parallel operation of multiple generator sets is often employed in certain systems under different working conditions. To maintain stability within the parallel system, the allocation of reactive power between the generators must be properly managed, a task regulated by excitation control mechanisms [30,31]. In the context of excitation control research, Patel et al. [32] proposed an alternative method based on command filtered backstepping principles to control the terminal voltage and stabilize the DG through the excitation system. In addition to the aforementioned approach, researchers have explored the integration of various advanced control techniques into excitation control. Examples include the decentralized improved cooperative excitation controller [33], the excitation controller based on linear matrix inequality (LMI) [34], robust control strategies [35,36], and model predictive control [37], all of which aim to improve system performance. However, it is worth noting that some controllers developed using these methods rely on linear approximations and bounded operating ranges. Consequently, their performance may degrade significantly in the presence of large disturbances [38].

The dynamic process of DGs in the system includes both the electromagnetic dynamic process and dynamic mechanical process, and the two are related to each other [39]. The comprehensive control of speed and excitation can be used as an effective measure to improve the transient stability of the MG system [40]. However, most of the existing DG strategies only consider one of these methods while ignoring the dual control functions of voltage regulation and prime mover speed regulation. In the above studies, stable islanded MGs based on nonlinear control techniques for speed regulation and excitation robust controllers for DGs have been studied [41]. However, the speed regulation and robust excitation controller they designed is not intelligent; that is, the user manually selects the parameters of the robust controller, and no optimization is used to optimize the adjustable parameters.

This paper proposes a robust control method for DG speed and excitation based on the intelligent CPSOGSA, which is used in island MG with multiple load types. The CPSOGSA optimizes the parameters of the robust controller, and the CPSOGSA is introduced for the robust control of DG speed and excitation. The simulation results show that the method effectively suppressed oscillations under severe disturbances and uncertain conditions. The main innovations of this paper can be divided into the following categories:

- Based on the theory of direct feedback linearization, a nonlinear speed and excitation robust controller of a DG is designed;

- The intelligent CPSOGSA is applied to optimize the dynamic output function parameters of the robust controller, thus introducing the CPSOGSA for this problem solving multi-objective mixed H_2/H_∞ robust controller;
- The proposed method effectively suppresses frequency and voltage oscillations under various load disturbances and uncertainties;
- Excellent damping efficiency, especially low overshoot, steady-state error, and settling time.

This paper is organized as follows: In Section 2, the isolated MG structure supplied by DG studied in this paper is introduced, and the dynamic mathematical model of the DG is established in detail, respectively. Then, in Section 3, a speed and excitation robust controller is designed for the MG system's primary power source-DG. Section 4 presents the CPSOGSA and its application to robust controller optimization problems. Simulation studies are conducted in Section 5 to demonstrate the advantages of the new method. Finally, Section 6 concludes this paper.

2. Modeling of Diesel Generator and Its Loads

This section briefly introduces the nonlinear mathematical model of DG, which mainly consists of two parts: speed regulation and the excitation system of DG.

2.1. Modeling of Speed Control Part

As illustrated in Figure 2, the diesel engine in the DG serves as a power machine that converts the heat energy from diesel fuel into the mechanical energy required by the generator [42]. However, it is important to note that the main driving output torque of the diesel engine, denoted as M_1, is a pulsating torque [43]. This pulsating torque can be mathematically decomposed into a Fourier series, represented by the following equation:

$$M_1 = M_p + \sum_{f=1}^{\infty} M_f^0 sin(f\omega_0 t + \varphi_f) \tag{1}$$

where M_1 is the DE pulsating torque; M_p is the average torque of one cycle; M_f^0 is the fth harmonic torque amplitude; ω_0 is the harmonic torque angular velocity; and φ_f is the fth harmonic torque initial phase angle.

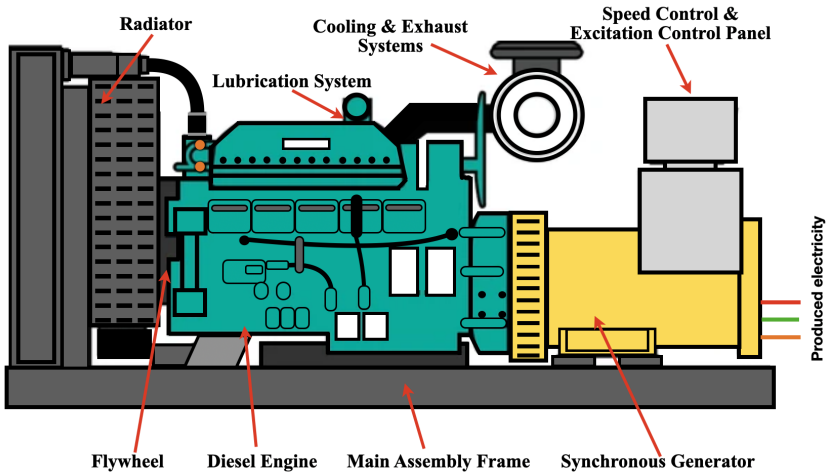

Figure 2. Principle diagram of DE speed regulation system.

As shown in Figure 3, a flywheel with a significant moment of inertia is installed on the main shaft of the diesel to keep the output torque of the diesel within the allowable range , which can make the flywheel rotation unevenness between (0.0033, 0.0067) [44]. During operation, the enormous flywheel torque ensures that the output torque of the

diesel is uniform. Therefore, the output torque's unevenness can be ignored in the diesel's regular operation. In other words, the first constant in Equation (1) can be retained, and the rest of the harmonic torque composed of amplitude, phase, and frequency can be ignored, and Equation (1) is derived

$$M_1 = M_p \tag{2}$$

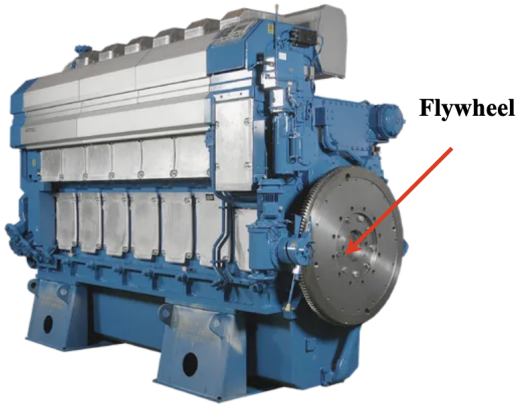

Figure 3. Flywheel of diesel.

The driving torque and rotating speed characteristics of DE are smooth curves, approximating several linear segments [45]. Divide the driving torque and rotating speed characteristics of the diesel into m sections; then, each section can be written as

$$M_{1j} = k_j n_d + b_j \tag{3}$$

where n_d is the DE rotational speed, and the constant value of k_j and b_j is determined by the positions of different segments ($j = 1, 2, \ldots, m$).

It can be seen from the adjustment characteristics of the diesel that the relationship between the main driving torque M_1 of the DE and the output throttle displacement L of the actuator presents a specific linear relationship [46]. At the same time, the driving torque of the diesel has a certain lag, so the adjustment characteristic of the diesel can be expressed as

$$M_1 = \frac{M_1^e}{L_e - L_0}(L(t - T_d) - L_0) \tag{4}$$

where M_1^e is the torque at rated oil supply; L_e is the rated stroke of the DE actuator; L_0 is the no-load stroke of the DE actuator; and T_d is the DE torque lag time.

Through the above analysis and derivation, the rotating speed characteristic and adjustment characteristic of the integrated the DE can be obtained as the expression of the driving torque M_1:

$$M_1 = k_j n_d + b_j + \frac{M_1^e}{L_e - L_0}(L(t - T_d) - L_0) \tag{5}$$

When the DE is running at the rated speed, the segment described in Equation (5) can be described as

$$M_1 = k_1 n_d + b_1 + \frac{M_1^e}{L_e - L_0}(L(t - T_d) - L_0) \tag{6}$$

Define $d_1 = b_1 - (M_1^e L_0)/(L_e - L_0)$; then, Equation (6) can be written as

$$M_1 = k_1 n_d + d_1 + \frac{M_1^e}{L_e - L_0} L(t - T_d) \tag{7}$$

The rotational speed, the number of cylinders, and the number of strokes of the diesel determine the torque lag time T_d of the diesel [47]. Generally, the following equation can be used to estimate the value range

$$\frac{15}{n_d} < T_d < \frac{15}{n_d} + \frac{60\tau}{n_d l_s} \tag{8}$$

where τ is the DE stroke coefficient and l_s is the number of DE cylinders.

The diesel parameters studied in this paper are the value of rated speed n_d = 1500 r/min, the number of cylinders is 16, and the stroke coefficient $\tau = 2$. According to Equation (8), the value range of T_d can be calculated as $0.01s < T_d < 0.015$. The speed transition time of the diesel is 2 s, and T_d is very small compared with it and can be ignored. Therefore, Equation (7) can become

$$M_1 = k_1 n_d + d_1 + \frac{M_1^e}{L_e - L_0} L \tag{9}$$

where L is the throttle actuator displacement.

The relationship between the rotational speed of the diesel n_d and the angular velocity of the crank shaft ω_g is

$$n_d = \frac{60\omega_g}{2\pi} \tag{10}$$

where ω_g is the angular velocity of the crankshaft shaft.

Equation (9) can be written as

$$M_1 = \frac{60k_1\omega_g}{2\pi} + d_1 + \frac{M_1^e}{L_e - L_0} L \tag{11}$$

The dynamic motion equation of the main shaft of the DG set can be expressed as

$$\dot{\omega}_g = \frac{1}{J}(M_1 - M_2 - M_d) \tag{12}$$

where J is the DE rotational moment of inertia; ω_g is the DE spindle angular velocity; M_1 is the DE output shaft torque; M_2 is the DE load torque; and M_d is the generator damping torque.

The damping torque M_d is generated by the damping winding of the synchronous generator, and its characteristic is that it is proportional to the electrical angular speed of the generator rotor, which can be calculated by Equation (13).

$$M_d = Dp\omega_g \tag{13}$$

where D is the damping factor and p is the number of synchronous generator pole pairs.

Substituting Equations (11) and (13) into Equation (12), we obtain

$$J\dot{\omega}_g + Dp\omega_g = \frac{60k_1\omega_g}{2\pi} + d_1 + \frac{M_1^e}{L_e - L_0} L - M_2 \tag{14}$$

General variables are marked per unit value in the research and analysis of electric power systems. In order to unify the form, Equation (14) can be standardized as per the unit value. This paper converts the mechanical angular speed into electrical angular speed and then standardizes the power, torque, and angular speed to study the speed response of the diesel. This paper defines the rated apparent power S_B of the DG as the reference value of power and defines $\omega_0 = 100\pi$ as the reference value of the angular speed. Therefore, in standardized form, Equation (14) can be written as

$$\frac{J\omega_{g0}^2}{S_B}\dot{\omega} = \frac{60k_1\omega_{g0}^2 - 2\pi Dp\omega_{g0}^2}{2\pi S_B}\omega + \frac{d_1\omega_{g0}}{S_B} + \frac{a\omega_{g0}}{S_B} L - M_2 \tag{15}$$

where ω_{g0} is $100\pi/p$; $a = \frac{M_1^e}{L_e - L_0}$.

Ignoring the no-load torque and the winding loss, M_2 is equal to the output torque of the synchronous generator. In the stability analysis or control system design, for the convenience of calculation, it is considered that the angular speed ω does not change much during the transient process and is approximately equal to the synchronous speed, that is, $\omega \approx 1$. Therefore, Equation (15) can be derived as

$$\frac{J\omega_{g0}^2}{S_B}\dot{\omega} = \frac{60k_1\omega_{g0}^2 - 2\pi Dp\omega_{g0}^2}{2\pi S_B}\omega + \frac{d_1\omega_{g0}}{S_B} + \frac{a\omega_{g0}}{S_B}L - P_e \tag{16}$$

The output power P_e of the salient-pole synchronous generator can be described as

$$P_e = \frac{E_q' U}{X_d'}\sin\delta + \frac{U^2}{2}\frac{X_d' - X_q}{X_d' X_q}sin(2\delta) \tag{17}$$

where E_q' is the q-axis transient potential; U is the DG terminal voltage; and X is the generator winding reactance.

The relationship between the generator rotor angle δ and the electrical angular velocity ω can be described as

$$\dot{\delta} = (\omega - 1)\omega_0 \tag{18}$$

where ω is the nominal value, δ and t are the actual values, and $\omega_0 = 100\pi$.

From Equations (16)–(18), the mathematical model of the electrical transient process of DGs is

$$\begin{cases} \dot{\delta} = (\omega - 1)\omega_0 \\ \dot{\omega} = \dfrac{T_b}{T_a}\omega + \dfrac{1}{T_a}c_1 + \dfrac{c_2}{T_a}L - \\ \qquad \dfrac{1}{T_a}\dfrac{E_q' U}{X_d'}\sin\delta - \dfrac{1}{T_a}\dfrac{U^2}{2}\dfrac{X_d' - X_q}{X_d' X_q}\sin(2\delta) \end{cases} \tag{19}$$

in the above, the definitions of T_a, T_b, c_1, c_2, and a are as follows:

$$\begin{cases} T_a = \dfrac{J\omega_{g0}^2}{S_B} \\ T_b = \dfrac{60k_1\omega_{g0}^2 - 2\pi Dp\omega_{g0}^2}{2\pi S_B} \\ c_1 = \dfrac{d_1\omega_{g0}}{S_B} \\ c_2 = \dfrac{a\omega_{g0}}{S_B} \\ a = \dfrac{M_1^e}{L_e - L_0} \end{cases}$$

2.2. Modeling of Excitation Control Part

During the operation of DGs, excitation control is the most basic and indispensable. The synchronous generator is the control object of the excitation control system [46]. Studying the dynamic characteristics of the excitation system is inseparable from the analysis of the dynamic characteristics of the synchronous generator. The mathematical model of the electromagnetic transient process of the DG includes the stator voltage balance equation of the generator and the transient electromagnetic equation of each winding of the rotor [48].

The standard form of the transient electromagnetic equation of the synchronous generator can be described as

$$\begin{cases} \dot{E}'_q = \dfrac{1}{T_{d0}} E_{fd} - \dfrac{1}{T_{d0}} E'_q - \dfrac{X_d - X'_d}{T_{d0}} \\ \dot{E}''_q = \dfrac{1}{T_{d0}} \dfrac{X''_d - X_l}{X'_d - X_l} E_{fd} + \left(\dfrac{1}{T''_{d0}} - \dfrac{X''_d - X_l}{X'_d - X_1} \dfrac{1}{T_{d0}} \right) E'_q \\ - \dfrac{1}{T''_{d0}} E''_q - \left(\dfrac{X'_d - X''_d}{T''_{d0}} + \dfrac{X''_d - X_l}{X'_d - X_l} \dfrac{X_d - X'_d}{T_{d0}} I_d \right) \\ \dot{E}''_d = -\dfrac{1}{T''_{q0}} E''_d + \dfrac{X_q - X''_q}{T''_{q0}} I_q \\ U_d = -RI_d + \omega X''_q I_q + \omega E''_d \\ U_q = -RI_q - \omega X''_d I_d + \omega E''_q \\ U = \sqrt{U_d^2 + U_q^2} \end{cases} \tag{20}$$

where U is the stator winding terminal voltage; U_d and U_q are the d-axis and q-axis components of the stator winding terminal voltage; R is the stator winding resistance; X is the winding reactance; I is the winding current; T is the winding time constant; E''_d is the d-axis subtransitory potential; E'_q is the q-axis transient potential; E''_q is the q-axis subtransitory potential; and E_{df} is the excitation winding voltage.

By combining Equations (19) and (20), a nonlinear mathematical model of the DG is obtained. This model reflects the interaction and mutual influence of speed and voltage and more accurately describes the change law of speed and voltage.

3. Design of Nonliear H_2/H_∞ Synthetic Controller

3.1. Multi-Objective State-Feedback Theory

The control system shown in Figure 4 defines the closed-loop transfer function $T_\infty(s)$ from disturbance w to H_∞ control performance output vector z_∞, and the closed-loop transfer function $T_2(s)$ from disturbance w to H_2 control performance output vector z_2. The control goal is to design a state feedback control law $u = Kx$ to stabilize the closed-loop system progressively. In addition, it needs to:

- Keep the RMS gain (H_∞ norm) of $T_\infty(s)$ below a certain specified value $\gamma_0 > 0$;
- Maintain the H_2 norm (LQG cost) of $T_2(s)$ below a certain specified value $v_0 > 0$;
- Minimized the form of H_2/H_∞ trade-off standard $\alpha T_2(s) + \beta T_\infty(s)$;
- Place the closed-loop pole in the designated area of the open left half-plane.

The mixed H_2/H_∞ standard considers both the interference suppression aspect (RMS gain from w to z_∞) and the LQG aspect (H_2 norm from w to z_2). In addition, the closed-loop pole can be forced into a specific part of the stable half-plane to obtain a well-damped transient response. Such control problems are called H_2/H_∞ control design problems [48,49].

The linear system shown in Figure 4 can be expressed as:

$$\begin{cases} \dot{x} = \boldsymbol{A}x + \boldsymbol{B}_1 w + \boldsymbol{B}_2 u \\ z_\infty = \boldsymbol{C}_1 x + \boldsymbol{D}_{11} w + \boldsymbol{D}_{12} u \\ z_2 = \boldsymbol{C}_2 x + \boldsymbol{D}_{21} w + \boldsymbol{D}_{22} u \end{cases} \tag{21}$$

where the first term in Equation (21) is a dynamic linear state-space differential equation and the second and third terms are its dynamic performance evaluation signals.

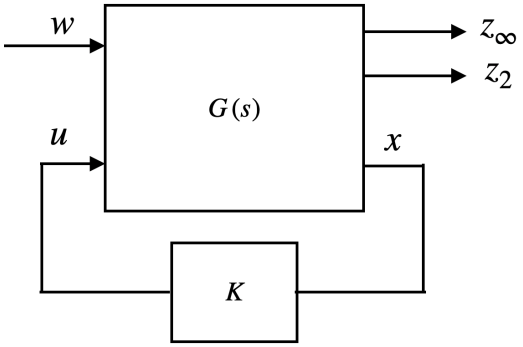

Figure 4. State-feedback control.

The closed-loop system formed after adding the controller $\boldsymbol{K}x$ can be described in the form of state-space as

$$\begin{cases} \dot{x} = \boldsymbol{A}_{cl}x + \boldsymbol{B}_1 w \\ z_\infty = \boldsymbol{C}_{cl1}x + \boldsymbol{D}_{11}w \\ z_2 = \boldsymbol{C}_{cl2}x + \boldsymbol{D}_{21}w \end{cases} \tag{22}$$

where $\boldsymbol{A}_{cl} = \boldsymbol{A} + \boldsymbol{B}_2\boldsymbol{K}$; $\boldsymbol{C}_{cl1} = \boldsymbol{C}_1 + \boldsymbol{D}_{12}\boldsymbol{K}$; $\boldsymbol{C}_{cl2} = \boldsymbol{C}_2 + \boldsymbol{D}_{22}\boldsymbol{K}$.

Taken separately, the two design goals have the following LMI formulation:

The H_∞ performance: the closed-loop RMS gain from w to z_∞ does not exceed γ if and only if there exists a symmetric matrix X_∞ such that

$$\begin{cases} \begin{bmatrix} \boldsymbol{A}_{cl}\boldsymbol{X}_\infty + \boldsymbol{X}_\infty\boldsymbol{A}_{cl}^T & \boldsymbol{B}_1 & \boldsymbol{X}_\infty\boldsymbol{C}_{cl1}^T \\ \boldsymbol{B}_1^T & -\gamma\boldsymbol{I} & \boldsymbol{D}_{11}^T \\ \boldsymbol{C}_{cl1}\boldsymbol{X}_\infty & \boldsymbol{D}_{11} & -\gamma\boldsymbol{I} \end{bmatrix} < 0 \\ \boldsymbol{X}_\infty > 0 \end{cases} \tag{23}$$

The H_2 performance: the closed-loop H_2 norm of $T_2(s)$ does not exceed v if there exist two symmetric matrices $\boldsymbol{X}_2$ and $\boldsymbol{Q}$ such that

$$\begin{cases} \begin{bmatrix} \boldsymbol{A}_{cl}\boldsymbol{X}_2 + \boldsymbol{X}_2\boldsymbol{A}_{cl}^T & \boldsymbol{B}_1 \\ \boldsymbol{B}_1^T & -\boldsymbol{I} \end{bmatrix} < 0 \\ \begin{bmatrix} \boldsymbol{Q} & \boldsymbol{C}_{cl2}\boldsymbol{X}_2 \\ \boldsymbol{X}_2\boldsymbol{C}_{cl2}^T & \boldsymbol{X}_2 \end{bmatrix} > 0 \\ Trace(\boldsymbol{Q}) < v^2 \end{cases} \tag{24}$$

The mixed H_2/H_∞ performance: the pole of the closed-loop system is located in the left half-open complex plane, and the performance index $\alpha\|T(s)_\infty\|_\infty^2 + \beta\|T_2(s)\|_2^2$ is minimized.

To solve the mixed objective, the two sets of conditions add up to a non-convex optimization problem with variables $\boldsymbol{Q}$, $\boldsymbol{K}$, $\boldsymbol{X}_\infty$, and $\boldsymbol{X}_2$. In order to facilitate the processing of this problem in the LMI framework, we seek a single Lyapunov matrix $\boldsymbol{X} := \boldsymbol{X}_\infty = \boldsymbol{X}_2$ to force the solution of the two goals. With the change of variable $\boldsymbol{Y} := \boldsymbol{K}\boldsymbol{X}$, this leads to the multi-objective state feedback synthesis problem, which the following sub-optimal LMI formula can express:

Minimize $\alpha\gamma^2 + \beta Trace(\boldsymbol{Q})$ over $\boldsymbol{Y}$, $\boldsymbol{X}$, $\boldsymbol{Q}$, and γ^2 satisfying:

$$\begin{cases} \begin{bmatrix} \boldsymbol{AX} + \boldsymbol{XA}^T + \boldsymbol{B}_2\boldsymbol{Y} + \boldsymbol{Y}^T\boldsymbol{B}_2^T & \boldsymbol{B}_1 & \boldsymbol{XC}_1^T + \boldsymbol{Y}^T\boldsymbol{D}_{12}^T \\ \boldsymbol{B}_1^T & -\gamma\boldsymbol{I} & \boldsymbol{D}_{11}^T \\ \boldsymbol{C}_1\boldsymbol{X} + \boldsymbol{D}_{12}\boldsymbol{Y} & \boldsymbol{D}_{11} & -\gamma\boldsymbol{I} \end{bmatrix} < 0 \\ \begin{bmatrix} \boldsymbol{Q} & \boldsymbol{C}_2\boldsymbol{X} + \boldsymbol{D}_{22}\boldsymbol{Y} \\ \boldsymbol{XC}_2^T + \boldsymbol{Y}^T\boldsymbol{D}_{22}^T & \boldsymbol{X} \end{bmatrix} < 0 \\ Trace(\boldsymbol{Q}) < v_0^2 \\ \gamma_0 < \gamma_0^2 \end{cases} \tag{25}$$

Denoting the optimal solution by $(\boldsymbol{X}^*, \boldsymbol{Y}^*, \boldsymbol{Q}^*, \gamma^*)$, the corresponding state-feedback gain is given by:

$$\boldsymbol{K}^* = \boldsymbol{Y}^*(\boldsymbol{X}^*)^{-1} \tag{26}$$

this gain guarantees the worst-case performances:

$$\begin{cases} \|T(s)_\infty\|_\infty \le \gamma^* \\ \|T(s)_2\|_2 \le \sqrt{Trace(\boldsymbol{Q}^*)} \end{cases} \tag{27}$$

The solution of the mixed H_2/H_∞ controller is usually configured with $\alpha = 0.5$ and $\beta = 0.5$ to obtain [46]. The robust controller obtained by this method can improve and optimize the control performance of the related system.

3.2. Design of Speed Controller

The schematic diagram of the DG integrated control system based on the nonlinear H_2/H_∞ integrated controller is shown in Figure 5. The DG integrated control system comprises a diesel, generator, nonlinear H_2/H_∞ integrated controller, actuator, fuel supply mechanism, and exciter. The nonlinear H_2/H_∞ integrated controller consists of two parts: one part is the nonlinear H_2/H_∞ speed controller, and the other is the nonlinear H_2/H_∞ voltage controller. The nonlinear H_2/H_∞ integrated controller should consider the coupling effect of speed and voltage, comprehensively control the speed and voltage, and control the mutual influence between the two to a minimum. Further, it should improve the stability of the frequency and voltage of the independent MG system.

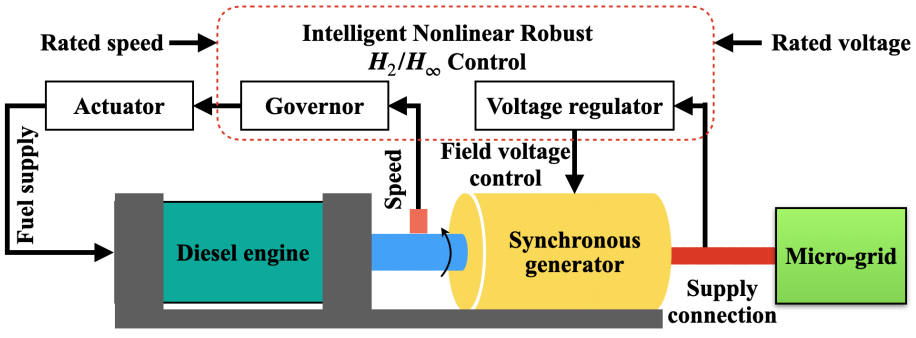

Figure 5. Principle diagram of diesel-generator set synthetic control system.

The differential equation expression of the actuator is:

$$\dot{L} = -\frac{1}{T_1}L + \frac{K_1}{T_1}u_1 \tag{28}$$

where T_1 is the actuator time constant and K_1 is the actuator gain.

The expression of the differential equation of the exciter is

$$\dot{E}_{fd} = -\frac{1}{T_2}E_{fd} + \frac{K_2}{T_2}u_2 \tag{29}$$

where T_2 is the exciter time constant and K_2 is the exciter gain.

By combining Equations (19) and (28), we can obtain the nonlinear mathematical model of the DG's speed control system:

$$\begin{cases} \dot{\delta} = (\omega - 1)\omega_0 \\ \dot{L} = -\dfrac{1}{T_1}L + \dfrac{K_1}{T_1}u_1 \\ \dot{\omega} = \dfrac{T_b}{T_a}\omega + \dfrac{1}{T_a}c_1 + \dfrac{c_2}{T_a}L - \dfrac{1}{T_a}\dfrac{E'_q U}{X'_d}\sin\delta - \\ \quad \dfrac{1}{T_a}\dfrac{U^2}{2}\dfrac{X'_d - X_q}{X'_d X_q}\sin(2\delta) \end{cases} \tag{30}$$

Equation (30) has apparent nonlinear terms. In order to be able to apply the above mixed H_2/H_∞ control theory, this paper uses the direct feedback linearization method to linearize the nonlinear mathematical model of the DG speed system described in Equation (30) to obtain its linear model and then obtain the corresponding nonlinear speed control law.

Three variables (X_1, X_2, and X_3) are defined in this paper, which can be expressed as:

$$\begin{cases} X_1 = \delta \\ X_2 = (\omega - 1)\omega_0 \\ X_3 = \dfrac{T_b}{T_a}\omega + \dfrac{1}{T_a}c_1 + \dfrac{c_2}{T_a}L - \dfrac{1}{T_a}\dfrac{E'_q U}{X'_d}\sin\delta \\ \quad \dfrac{1}{T_a}\dfrac{U^2}{2}\dfrac{X'_d - X_q}{X'_d X_q}\sin(2\delta) \end{cases} \tag{31}$$

According to the definitions of X_1, X_2 and X_3, the nonlinear differential equations described by Equation (30) can be rewritten as:

$$\begin{cases} \dot{X}_1 = X_2 \\ \dot{X}_2 = \omega_0 X_3 + d_1 W \\ \dot{X}_3 = \dfrac{T_b}{T_a}X_3 + \dfrac{c_2 K_1}{T_a T_1}u_1 - \dfrac{c_2}{T_a T_1}L - \\ \quad \dfrac{E'_q U\omega_0}{T_a X'_d}\cos\delta(\omega - 1) - \\ \quad \dfrac{U^2\omega_0(X'_d - X_q)}{T_a X'_d X_d}\cos(2\delta)(\omega - 1) \end{cases} \tag{32}$$

where $d_1 W$ is the disturbance signal set when the mixed H_2/H_∞ control method is adopted, including equivalent disturbances caused by disturbance torque and modelling errors.

For speed control, this paper defines virtual control variables V as:

$$\begin{aligned} V = &\frac{c_2 K_1}{T_a T_1}u_1 - \frac{c_2}{T_a T_1}L - \frac{E'_q U\omega_0}{T_a X'_d}\cos\delta(\omega - 1) - \\ &\frac{U^2\omega_0(X'_d - X_q)}{T_a X'_d X_q}\cos(2\delta)(\omega - 1) \end{aligned} \tag{33}$$

By introducing virtual control variables V, Equation (30) is described by linear state-space differential equations as:

$$\dot{X} = \boldsymbol{A}_s X + \boldsymbol{B}_{1s} W + \boldsymbol{B}_{2s} V \tag{34}$$

where X, $\boldsymbol{A}_s$, $\boldsymbol{B}_{1s}$ and $\boldsymbol{B}_{2s}$ are defined as follows:

$$X = \begin{bmatrix} X_1 \\ X_2 \\ X_3 \end{bmatrix}; \boldsymbol{A}_s = \begin{bmatrix} 0 & 1 & 0 \\ 0 & 0 & \omega_0 \\ 0 & 0 & \dfrac{T_b}{T_a} \end{bmatrix};$$
$$\boldsymbol{B}_{1s} = \begin{bmatrix} 0 \\ d_1 \\ 0 \end{bmatrix}; \boldsymbol{B}_{2s} = \begin{bmatrix} 0 \\ 0 \\ 1 \end{bmatrix}.$$

Add the dynamic performance evaluation signal described by Equation (35) to this system

$$\begin{cases} Z_{\infty s} = \boldsymbol{C}_{1s} X + \boldsymbol{D}_{11s} W + \boldsymbol{D}_{12s} V \\ Z_{2s} = \boldsymbol{C}_{2s} X + \boldsymbol{D}_{21s} W + \boldsymbol{D}_{22s} V \end{cases} \tag{35}$$

where

$$\boldsymbol{C}_{1s} = \begin{bmatrix} q_{11} & 0 & 0 \\ 0 & q_{12} & 0 \\ 0 & 0 & q_{13} \end{bmatrix}; \boldsymbol{D}_{12s} = \begin{bmatrix} 0 \\ 0 \\ r_1 \end{bmatrix};$$
$$\boldsymbol{C}_{2s} = \begin{bmatrix} q_{21} & 0 & 0 \\ 0 & q_{22} & 0 \\ 0 & 0 & q_{23} \end{bmatrix}; \boldsymbol{D}_{22s} = \begin{bmatrix} 0 \\ 0 \\ r_2 \end{bmatrix};$$
$$\boldsymbol{D}_{11s} = \boldsymbol{D}_{21s} = \begin{bmatrix} 0 \\ 0 \\ 0 \end{bmatrix}.$$

$\boldsymbol{C}_{1s}$, $\boldsymbol{C}_{2s}$, $\boldsymbol{D}_{11s}$, $\boldsymbol{D}_{12s}$, $\boldsymbol{D}_{21s}$, and $\boldsymbol{D}_{22s}$ are weighting matrices, $q_{ij} > 0$ ($i = 1, 2$; $j = 1, 2, 3$) and $r_i > 0$ ($i = 1, 2$) are weighting coefficients. A controller that meets the optimal performance requirements can be obtained by selecting different weighting coefficients. The performance requirements include the independent power system stability, frequency adjustment accuracy, and low energy consumption of the speed control system.

From Equations (34) and (35), the augmented controlled object based on the mixed H_2/H_∞ control theory can be obtained as

$$\boldsymbol{P}_s = \begin{bmatrix} \boldsymbol{A}_s & \boldsymbol{B}_{1s} & \boldsymbol{B}_{2s} \\ \boldsymbol{C}_{1s} & \boldsymbol{D}_{11s} & \boldsymbol{D}_{12s} \\ \boldsymbol{C}_{2s} & \boldsymbol{D}_{21s} & \boldsymbol{D}_{22s} \end{bmatrix} \tag{36}$$

Bring the augmented controlled object $\boldsymbol{P}_s$ into the framework shown in Figure 4 and meet the design requirements of the multi-objective H_2/H_∞ state-feedback controller at the same time, and then the H_2/H_∞ state feedback controller can be obtained as:

$$\begin{aligned} V =& \boldsymbol{F}_s X \\ =& \begin{bmatrix} f_{1s} & f_{2s} & f_{3s} \end{bmatrix} \begin{bmatrix} X_1 \\ X_2 \\ X_3 \end{bmatrix} \\ =& f_{1s} X_1 + f_{2s} X_2 + f_{3s} X_3 \end{aligned} \tag{37}$$

From Equations (33) and (37), the speed control law u_1 can be solved as:

$$\begin{aligned} u_1 =& \frac{1}{K_1}L + \frac{T_a T_1}{c_2 K_1}\boldsymbol{F}_s X + \frac{E'_q U \omega_0 T_1}{c_2 K_1 X'_d}\cos\delta(\omega - 1) \\ &+ \frac{U^2 \omega_0 T_1 (X'_d - X_q)}{c_2 K_1 X'_d X_q}\cos(2\delta)(\omega - 1) \end{aligned} \tag{38}$$

Substituting X_1, X_2, and X_3 into Equation (38), the DE nonlinear H_2/H_∞ speed control law in the usable form shown in Equation (39) can be obtained.

$$\begin{aligned} u_1 =& \frac{1}{K_1}L + \frac{T_a T_1}{c_2 K_1}f_{1s}\delta + \frac{T_a T_1}{c_2 K_1}f_{2s}(\omega - 1)\omega_0 + \\ & \frac{T_b T_1}{c_2 K_1}f_{3s}\omega - \frac{T_1}{c_2 K_1}\frac{E'_q U}{X'_d}f_{3s}\sin\delta - \\ & \frac{T_1}{c_2 K_1}\frac{U^2}{2}\frac{X'_d - X_q}{X'_d X_q}f_{3s}\sin(2\delta) + \frac{T_1}{c_2 K_1}f_{3s}c_1 + \\ & \frac{T_1}{K_1}f_{3s}L + \frac{E'_q U \omega_0 T_1}{c_2 K_1 X'_d}\cos\delta(\omega - 1) + \\ & \frac{U^2 \omega_0 T_1 (X'_d - X_q)}{c_2 K_1 X'_d X_q}\cos(2\delta)(\omega - 1) \end{aligned} \tag{39}$$

3.3. Design of Excitation Control Controller

By combining Equations (20) and (29) of the first three terms, one can obtain the nonlinear mathematical model of the synchronous generator voltage regulation system, which is shown in Equation (40).

$$\begin{cases} \dot{E}_{fd} = -\dfrac{1}{T_2}E_{fd} + \dfrac{K_2}{T_2}u_2 \\ \dot{E}'_q = \dfrac{1}{T_{d0}}E_{fd} - \dfrac{1}{T_{d0}}E'_q - \dfrac{X_d - X'_d}{T_d}I_d \\ \dot{\delta} = (\omega - 1)\omega_0 \\ \dot{\omega} = \dfrac{T_b}{T_a\omega_0}\omega + \dfrac{1}{T_a\omega_0}c_1 + \dfrac{c_2}{T_a\omega_0}L - \\ \dfrac{1}{T_a\omega_0}\dfrac{E'_q U}{X'_d}\sin\delta - \dfrac{1}{T_a\omega_0}\dfrac{U^2}{2}\dfrac{X'_d - X_q}{X'_d X_q}\sin(2\delta) \end{cases} \tag{40}$$

Since the damper winding of the synchronous generator has a weak influence on the excitation control, the fourth and fifth terms of Equation (20) can be ignored when designing the voltage controller. Regarding the electromagnetic power P_e as an external disturbance, Equation (40) becomes

$$\begin{cases} \dot{E}_{fd} = -\dfrac{1}{T_2}E_{fd} + \dfrac{K_2}{T_2}u_2 \\ \dot{E}'_q = \dfrac{1}{T_{d0}}E_{fd} - \dfrac{1}{T_{d0}}E'_q - \dfrac{X_d - X'_d}{T_{d0}}I_d \\ \dot{\delta} = \omega - 1 \\ \dot{\omega} = \dfrac{T_b}{T_a\omega_0}\omega + \dfrac{1}{T_a\omega_0}c_1 + \dfrac{c_2}{T_a\omega_0}L - \dfrac{1}{T_a\omega_0}P_e \end{cases} \tag{41}$$

Since E'_q is not easy to measure, it is not conducive to designing a state feedback controller. Therefore, the voltage error ΔU is selected as the state variable, so this paper

converts Eq' in Equation (41) into ΔU by a constant c_3. According to the relationship between variable data:

$$U = E'_q - c_3\delta \tag{42}$$

Through the relationship between U and the voltage U_0 at the stator winding end of the generator, it can be derived:

$$E'_q = U_0 + \Delta U + c_3\delta \tag{43}$$

According to the relationship described in Equation (43), the state-space differential equation expressed by Equation (41) can be rewritten as

$$\begin{cases} \dot{E}_{fd} = -\dfrac{1}{T_2}E_{fd} + \dfrac{K_2}{T_2}u_2 \\ \Delta\dot{U} = \dfrac{1}{T_{d0}}E_{fd} - \dfrac{1}{T_{d0}}\Delta U - \dfrac{1}{T_{d0}}c_3\delta - \\ \qquad c_3\omega + (c_3 - \dfrac{1}{T_{d0}}) - \dfrac{X_d - X'_d}{T_{d0}}I_d \\ \dot{\delta} = \omega - 1 \\ \dot{\omega} = \dfrac{T_b}{T_a\omega_0}\omega + \dfrac{1}{T_a\omega_0}c_1 + \dfrac{c_2}{T_a\omega_0}L - \dfrac{1}{T_a\omega_0}P_e \end{cases} \tag{44}$$

Equation (44) is written as a linear state-space differential equation in the form

$$\dot{X}' = \boldsymbol{A}_e X' + \boldsymbol{B}_{1e}W' + \boldsymbol{B}_{2e}u_2 \tag{45}$$

where

$$X'(t) = \begin{bmatrix} E_{fd} \\ \Delta U \\ \delta \\ \omega \end{bmatrix}; W' = \begin{bmatrix} I_d \\ L \\ P_e \\ 1 \end{bmatrix}; \boldsymbol{B}_{2e} = \begin{bmatrix} \dfrac{K_2}{T_2} \\ 0 \\ 0 \\ 0 \end{bmatrix};$$

$$\boldsymbol{A}_e = \begin{bmatrix} -\dfrac{1}{T_2} & 0 & 0 & 0 \\ \dfrac{1}{T_{d0}} & -\dfrac{1}{T_{d0}} & -\dfrac{c_3}{T_{d0}} & -c_3 \\ 0 & 0 & 0 & 1 \\ 0 & 0 & 0 & \dfrac{T_b}{T_a\omega_0} \end{bmatrix};$$

$$\boldsymbol{B}_{1e} = \begin{bmatrix} 0 & 0 & 0 & 0 \\ X_d - X'_d & 0 & 0 & c_3 - \dfrac{1}{T_{d0}} \\ -\dfrac{T_{d0}}{0} & 0 & 0 & -1 \\ 0 & \dfrac{c_2}{T_a\omega_0} & -\dfrac{1}{T_a\omega_0} & \dfrac{c_1}{T_a\omega_0} \end{bmatrix}.$$

Similarly, the dynamic performance evaluation signal of the system described in Equation (45) is defined as

$$\begin{cases} Z_{\infty e} = \boldsymbol{C}_{1e}X' + \boldsymbol{D}_{11e}W' + \boldsymbol{D}_{12e}u_2 \\ Z_{2e} = \boldsymbol{C}_{2e}X' + \boldsymbol{D}_{21e}W' + \boldsymbol{D}_{22e}u_2 \end{cases} \tag{46}$$

where

$$\boldsymbol{C}_{1e} = \begin{bmatrix} q_{14} & 0 & 0 & 0 \\ 0 & q_{15} & 0 & 0 \\ 0 & 0 & q_{16} & 0 \\ 0 & 0 & 0 & q_{17} \end{bmatrix}; \boldsymbol{D}_{12e} = \begin{bmatrix} r_3 \\ r_4 \\ r_5 \\ r_6 \end{bmatrix};$$

$$\boldsymbol{C}_{2e} = \begin{bmatrix} q_{24} & 0 & 0 & 0 \\ 0 & q_{25} & 0 & 0 \\ 0 & 0 & q_{26} & 0 \\ 0 & 0 & 0 & q_{27} \end{bmatrix}; \boldsymbol{D}_{22e} = \begin{bmatrix} r_7 \\ r_8 \\ r_9 \\ r_{10} \end{bmatrix};$$

$$\boldsymbol{D}_{11e} = \boldsymbol{D}_{21e} = \begin{bmatrix} 0 & 0 & 0 & 0 \\ 0 & 0 & 0 & 0 \\ 0 & 0 & 0 & 0 \\ 0 & 0 & 0 & 0 \end{bmatrix}.$$

$\boldsymbol{C}_{1e}$, $\boldsymbol{C}_{2e}$, $\boldsymbol{D}_{11e}$, $\boldsymbol{D}_{12e}$, $\boldsymbol{D}_{21e}$, and $\boldsymbol{D}_{22e}$ are weighting matrices, $q_{ij} > 0$ ($i = 1,2$; $j = 4,5,6,7$), and $r_i > 0 (i = 3,4,\ldots,10)$ are weighting coefficients. The voltage controller that meets the optimal performance is solved by combining different weighting coefficients. The performance includes the system stability, voltage regulation accuracy, and low energy loss of the excitation system.

From Equations (45) and (46), the augmented controlled object $\boldsymbol{P}_e$ used to solve the mixed H_2/H_∞ robust controller can be obtained, which can be expressed as:

$$\boldsymbol{P}_e = \begin{bmatrix} \boldsymbol{A}_e & \boldsymbol{B}_{1e} & \boldsymbol{B}_{2e} \\ \boldsymbol{C}_{1e} & \boldsymbol{D}_{11e} & \boldsymbol{D}_{12e} \\ \boldsymbol{C}_{2e} & \boldsymbol{D}_{21e} & \boldsymbol{D}_{22e} \end{bmatrix} \tag{47}$$

Similarly, the augmented controlled object $\boldsymbol{P}_e$ is brought into the solution framework shown in Figure 4, and the voltage H_2/H_∞ state feedback controller of the DG is obtained to satisfy the LMI. The nonlinear H_2/H_∞ voltage control law of the DG is

$$\begin{aligned} u_2 =& \boldsymbol{F}_e X' \\ =& \begin{bmatrix} f_{1e} & f_{2e} & f_{3e} & f_{4e} \end{bmatrix} \begin{bmatrix} E_{fd} \\ \Delta U \\ \delta \\ \omega \end{bmatrix} \\ =& f_{1e} E_{fd} + f_{2e} \Delta U + f_{3e} \delta + f_{4e} \omega \end{aligned} \tag{48}$$

Combining the Equations (39) and (48) derived above, the DG's nonlinear robust H_2/H_∞ integrated controller is obtained.

$$\begin{cases} u_1 = \dfrac{1}{K_1} L + \dfrac{T_a T_1}{c_2 K_1} f_{1s} \delta + \dfrac{T_a T_1}{c_2 K_1} f_{2s} (\omega - 1) \omega_0 + \\ \quad \dfrac{T_b T_1}{c_2 K_1} f_{3s} \omega - \dfrac{T_1}{c_2 K_1} \dfrac{E'_q U}{X'_d} f_{3s} \sin \delta - \\ \quad \dfrac{T_1}{c_2 K_1} \dfrac{U^2}{2} \dfrac{X'_d - X_q}{X'_d X_q} f_{3s} \sin(2\delta) + \dfrac{T_1}{c_2 K_1} f_{3s} c_1 + \\ \quad \dfrac{T_1}{K_1} f_{3s} L + \dfrac{E'_q U \omega_0 T_1}{c_2 K_1 X'_d} \cos \delta (\omega - 1) + \\ \quad \dfrac{U^2 \omega_0 T_1 (X'_d - X_q)}{c_2 K_1 X'_d X_q} \cos(2\delta)(\omega - 1) \\ u_2 = f_{1e} E_{fd} + f_{2e} \Delta U + f_{3e} \delta + f_{4e} \omega \end{cases} \tag{49}$$

It can be found from Equation (49) that the designed nonlinear control law considers the coupling effect of the DG's speed and voltage and comprehensively controls the two, which can improve the dynamic accuracy of the DG's speed and voltage. Further, it can improve the stability of the MG system connected to the DG.

4. Artificial Hybrid PSOGSA with Chaotic Maps Approach and Its Application to Multi-Objective H_2/H_∞ Robust Problem

4.1. The Proposed CPSOGSA Algorithm

The artificial intelligence CPSOGSA algorithm is a hybrid particle swarm optimization and gravitational search algorithm combined with chaotic mapping [50]. Moreover, the CPSOGSA is superior and more robust than other methods (such as MSA, GWO, WOA, and so on) [51]. Therefore, this paper also adopts CPSOGSA to optimize the robust controller. This subsection provides the necessary description of the algorithm.

4.1.1. Particle Swarm Optimization

The PSO consists of three crucial operators, which are the inertia weight vector w_p, the personal particle best (pbest), and the global particle best (gbest). The inertia weight gives diversification (exploration) capability, and <pbest, gbest> provides intensification (exploitation) power to PSO, respectively [52]. The velocity $v_i(k)$ and position $p_i(k)$ of each particle in the PSO algorithm are updated as follows:

$$\begin{cases} v_i(k+1) = w_p v_i(k) + c_1 \times \text{rand} \times (\text{pbest}_i - p_i(k)) \\ + c_2 \times \text{rand} \times (\text{gbest}_i - p_i(k)) \\ p_i(k+1) = p_i(k) + v_i(k+1) \end{cases} \tag{50}$$

where c_1 and c_2 are the acceleration coefficient and rand is a uniform random variable between O and 1.

4.1.2. Gravitational Search Algorithm

GSA is an optimization algorithm inspired by Newton's theories of gravity and motion. The operation steps of GSA are briefly summarized as follows [53].

Positions of N agents constituting the initialization population P_i in GSA are listed in Equation (51). The best and worst fitness values are computed for each iteration. The best and worst fitness values are defined as in Equation (52) for the problem.

$$P_i = \left(p_1^1, \ldots, p_i^d, \ldots, p_i^n\right), \quad i = 1, 2, \ldots, N \tag{51}$$

where p_i^d is the ith agent of the dth dimensions.

$$\begin{aligned} &\text{best}(k) = \min \text{fit}_i(k) \quad i \in \{1, 2, \ldots, N\} \\ &\text{worst}(k) = \max \text{fit}_i(k) \quad i \in \{1, 2, \ldots, N\} \end{aligned} \tag{52}$$

where $\text{fit}_i(k)$ denotes the fitness value of the ith individual.

The gravitational constant $G(k)$ for each iteration and inertial masses are calculated as follows:

$$\begin{cases} G(k) = G_0 e^{\left(-\alpha \frac{k}{K}\right)} \\ M_{ai} = M_{pi} = M_{ii} = M_i \quad i = 1, 2, 3, \ldots, N \\ m_i(k) = \dfrac{\text{fit}_i(k) - \text{worst}(k)}{\text{best}(k) - \text{worst}(k)} \\ M_i(k) = \dfrac{m_i(k)}{\sum_{j=1}^{N} m_j(k)} \end{cases} \tag{53}$$

where G_0 and α are the initial value of gravitational constant and the specified constant; k and K are the index and the total number of iterations; M_{ai} is the active mass at kth iteration

for the ith agent; M_{pi} is the passive mass at kth iteration for the ith agent; M_{ii} is the the inertial mass at kth iteration for the ith agent; and M_i is the mass at kth iteration for the ith agent.

The force $F_{ij}^d(k)$ acting on the ith mass from the jth mass, the total force $F_i^d(k)$, and the acceleration value $\sigma_i^d(k)$ at iteration k are calculated as follows:

$$\begin{cases} F_{ij}^d(k) = G(k)\dfrac{M_{pi}(k) \times M_{aj}(k)}{R_{ij}(k) + \varepsilon}\left(p_j^d(k) - p_i^d(k)\right) \\ F_i^d(k) = \displaystyle\sum_{j \in (k)\text{best}, j \neq i} \text{rand}_j F_{ij}^d(k) \\ \sigma_i^d(k) = \dfrac{F_i^d(k)}{M_{ii}(k)} \end{cases} \tag{54}$$

where R_{ij} is the euclidean distance between the ith mass and the jth mass.

The velocity $V_i^d(k)$ and position $p_i^d(k)$ of the ith agent at the dth dimension of the next iteration are updated as follows:

$$\begin{cases} V_i^d(k+1) = \text{rand} \times V_i^d(k) + \sigma_i^d(k) \\ p_i^d(k+1) = p_i^d(k) + V_i^d(k+1) \end{cases} \tag{55}$$

4.1.3. Modified Hybrid Particle Swarm Optimization and Gravitational Search Algorithm with Chaotic Maps

The hybrid PSOGSA combines the advantages of PSO and GSA algorithms. The algorithm can be explained a follows:

$$\begin{cases} V_i(k+1) = w_p \times V_i(k) + c_1' \times \text{rand} \times \sigma_i(k) \\ + c_2' \times \text{rand} \times (\text{gbest} - p_i(k)) \\ p_i(k+1) = p_i(k) + V_i(k+1) \end{cases} \tag{56}$$

When the chaotic map is used in the optimization algorithm, the optimization algorithm can quickly converge to the optimal solution and get rid of the optimal local solution [54]. Therefore, the one-dimensional and irreversible chaotic mapping method with this advantage is applied to the PSOGSA optimization algorithm so that the performance of PSOGSA can be further improved. The chaotic map equation gives these characteristics of the chaotic map. In [55], ten chaotic mapping methods are given to improve the performance of the hybrid PSOGSA algorithm, and the change curve of the chaotic map with the number of iterations is shown in Figure 6. From the figure, it can be found that there is no random value in any chaotic map.

In the proposed CPSOGSA algorithm, the chaotic map method is used to improve the local search ability of GSA. Equation (54) calculates the total force, while a random number between 0 and 1 is used as a weight. In other words, this parameter will impact the local search ability of the algorithm. If this situation is considered, using chaotic map methods instead of the random number could increase the convergence ability of the PSOGSA algorithm in an optimization process. Although each chaotic map follows the order in the Table, Equation (57) is applied instead of using a random parameter for calculating the total force in Equation (54). The application of chaotic map methods to the total force value is shown in Equation (57). After the total force value is calculated, the acceleration value is determined using Equation (53), while Equation (56) updates the velocities and positions of all agents in the population. In summary, the flowchart of the proposed CPSOGSA is shown in Figure 7.

$$F_i^d(k) = \sum_{j \in k\text{best}, j \neq i} C(k) F_{ij}^d(k) \tag{57}$$

where $C(k)$ is the chaotic sequence constant for the kth iteration.

In this paper, the Tent chaos mapping is used to calculate the value of $C(k)$ in the algorithm, and its computational mathematical expression is shown as follows:

$$C(k+1) = \begin{cases} 2C(k) & C(k) < 0.5 \\ 2(1-C(k)) & \text{else} \end{cases} \tag{58}$$

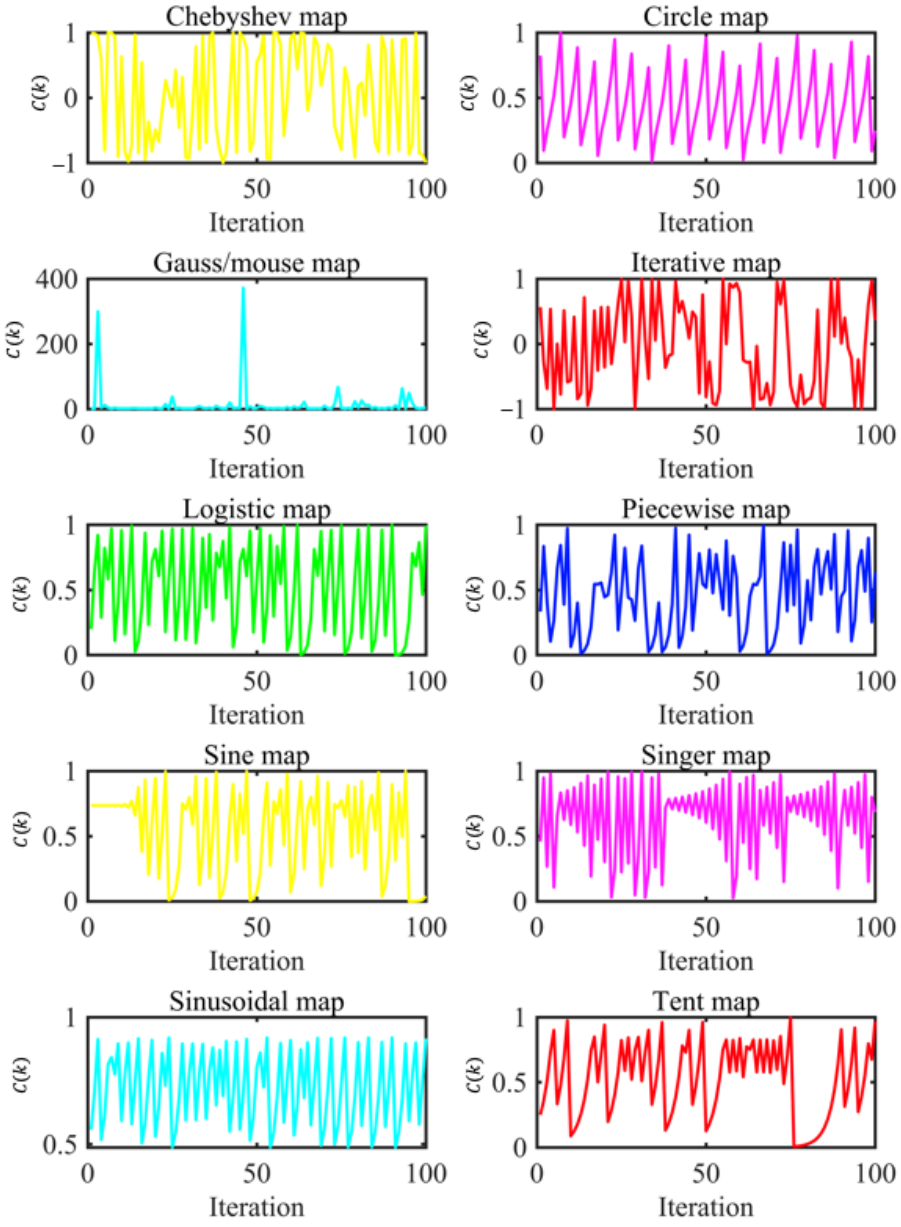

Figure 6. Curves of chaotic maps.

4.2. Applying CPSOGSA to Multi-Objective Robust H_2/H_∞ Problem

In subsection 3.2, the dynamic performance evaluation function and its weighting matrix for solving the robust controller of DG speed are proposed. The value of the weighting coefficient in these weighting matrices dramatically influences the performance of the speed controller. Therefore, these parameters need to be sufficient, and there are ten weighting coefficients for solving the speed robust controller, including the values of $q_{ij} > 0 (i = 1,2; j = 1,2,3)$, $r_i (i = 1,2)$. This paper uses the CPSOGSA algorithm to optimize and adjust these parameters. In optimizing the speed controller, the objective optimization function of CPSOGSA is OF_1. The function described by Equation (59) is used

to calculate the fitness value passed in the optimization process, aiming to minimize the absolute value of the change in the absolute value of the DG speed during this period.

$$OF_1 = \int |\Delta\omega|^2 dt \tag{59}$$

where $\Delta\omega$ is the speed deviation of DG.

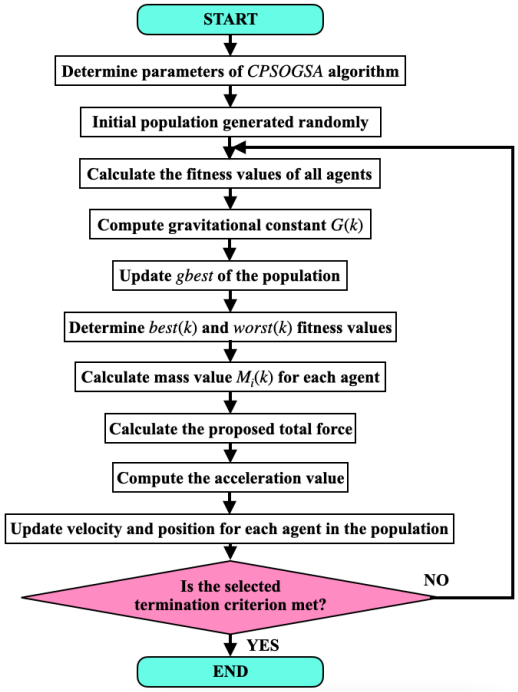

Figure 7. The flowchart of proposed CPSOGSA.

Similarly, CPSOGSA is used to adjust the dynamic performance evaluation function of the DG excitation controller proposed in subsection 3.3 and the weighting coefficients in the weighting matrix. For the solution of the excitation controller, the weighting coefficients include $q_{ij}(i = 1, 2; j = 4, 5, 6, 7)$, $r_i(i = 3, 4, \ldots, 10)$. In the optimization process, the objective optimization function of CPSOGSA is OF_2. The function described by Equation (60) is used to calculate the fitness value of the excitation controller during the optimization process, aiming to minimize the absolute value of the DG voltage in time.

$$OF_2 = \int |\Delta U|^2 dt \tag{60}$$

where ΔU is the voltage deviation of DG.

In conclusion, these parameters need to be adequately tuned. The number of parameters to be adjusted is 16. These parameters are optimally adjusted using the CPSOGSA algorithm, whose overall optimal objective function is considered to be Equation (61) as the weighted sum of OF_1 and OF_2 given by Equations (59) and (59). Therefore, the optimization objective can be described as

$$OF = min\{OF_1 + OF_2\} \tag{61}$$

5. Numerical Study

The MG system composed of DG is shown in Figure 8. Among them, the rated power of the DE is 1250 kW, the rated speed is 1500 r/min, the rated torque is 11.9 kNm, and the moment of inertia is 71.82, while the rated voltage of the generator is 380 V, the rated current is 2310 A, the power factor is 0.8, and the rated frequency is 50 Hz. In addition,

there are static and dynamic loads in this MG. The static load is mainly composed of electric heaters and lighting equipment, which accounts for a small proportion of the total loads; the dynamic loads refers to PMSM and driving devices, such as washing machines, water pumps, and fans, which account for a large proportion of the total load. Some parameters are also used for simulation, as shown in Table 1.

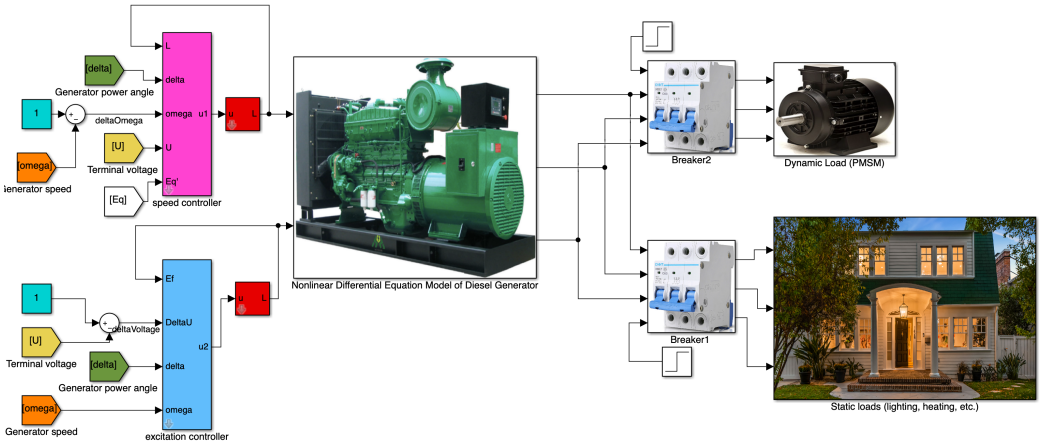

Figure 8. Diesel generator and its microgrid Simulink model.

Table 1. Relevant parameters for simulation.

T_a	T_b	c_1	c_2	X_d	X'_d
1.136	−0.492	1.515	−0.215	2.053	0.213
X_q	T_1	R	T_{d0}	K_1	d_1
1.003	0.050	0.011	2.200	0.200	0.1

5.1. Simulation Parameters

The selection of the relevant coefficients in the weighting function is a difficult point in the multi-objective H_2/H_∞ control and must be selected through repeated trials. After each trial selection, use the LMI toolbox to find the state feedback coefficient, substitute it into the simulation model, and then conduct the characteristic test to obtain the best comprehensive performance index. Simulations are carried out in MATLAB/Simulink and its programming environment interface. The parameters generated by the CPSOGSA algorithm are brought into the weighting function, and the state feedback control matrix $\boldsymbol{F}_s$ of the speed regulation part of the DG and the state feedback control matrix $\boldsymbol{F}_e$ of the excitation control part are calculated by the LMI and sent to Simulink. Simulink then iteratively evaluates the performance of the DG based on the adjusted parameters. In general, the flowchart of Figure 9 can be thought of as an optimization process. The number of iterative optimizations in this paper is 100.

As shown in Figure 10, under the optimization objective described in Equation (61), the fitness value (OF value) curve changes in different algorithm iterations 100 times . The optimization range of each parameter is $[1, 1e-3]$. It is not difficult to find from the figure that the CPSOGSA algorithm only needs about ten iterations to complete the optimization. On the contrary, the traditional algorithms are insufficient in terms of convergence and optimization efficiency. For example, the particle swarm algorithm PSO needs nearly 80 generations to converge, while the gravitational search algorithm falls into the local optimum at the beginning, and after introducing the chaotic sequence, GSA can avoid falling into the local optimum.

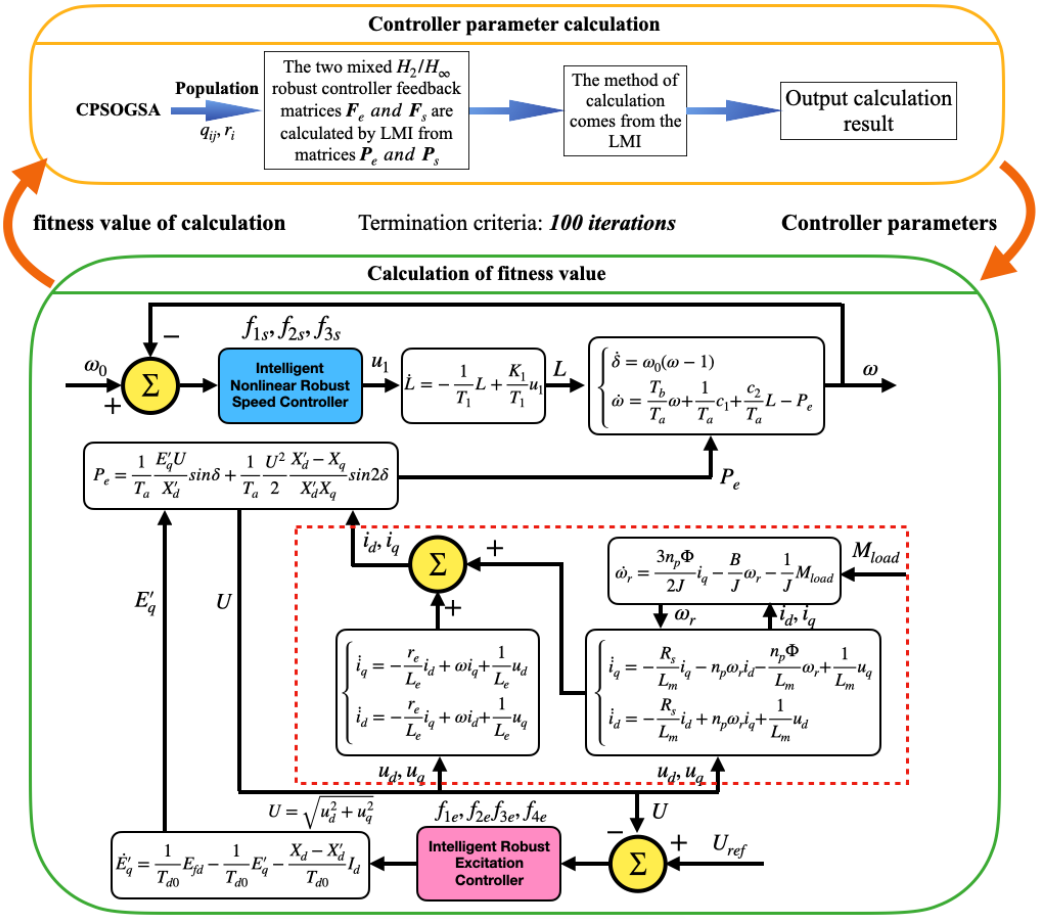

Figure 9. The flowchart of optimization process.

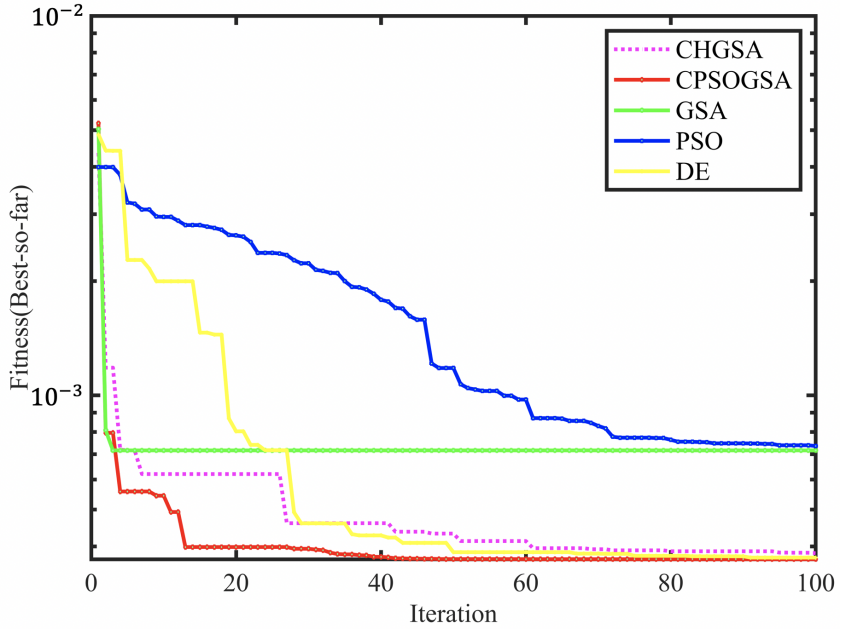

Figure 10. Iterative graph of the optimization process.

For the design of the speed control part of the nonlinear integrated controller based on the mixed H_2/H_∞ control theory, after the optimization of the CPSOGSA optimization algorithm, the weighting matrixs in Equation (35) are

$$\boldsymbol{C}_{1s} = \boldsymbol{C}_{2s}\begin{bmatrix} 0.4788 & 0 & 0 \\ 0 & 0.0015 & 0 \\ 0 & 0 & 0.1105 \end{bmatrix}$$

$$\boldsymbol{D}_{12s} = \boldsymbol{D}_{22s}\begin{bmatrix} 0 \\ 0 \\ 0.0011 \end{bmatrix}$$

Combining these matrices and using the linear matrix inequality toolbox in MATLAB, find the feedback coefficients in Equation (37) as $f_{1s} = -1.9188$, $f_{2s} = -1.8738$, and $f_{3s} = 35.604$.

Similarly, for the weighting matrix in Equation (46), these matrices are

$$\boldsymbol{C}_{1e} = \boldsymbol{C}_{2e} = \begin{bmatrix} 0.7817 & 0 & 0 & 0 \\ 0 & 3.824 \times 10^3 & 0 & 0 \\ 0 & 0 & 0.0256 & 0 \\ 0 & 0 & 0 & 0.1270 \end{bmatrix}$$

$$\boldsymbol{D}_{12e} = \boldsymbol{D}_{22e} = \begin{bmatrix} 0.1038 \\ 0.1143 \\ 0.1043 \\ 0.1417 \end{bmatrix}$$

Using the LMI toolbox in Matlab, obtain the coefficients of state-feedback controller in Equation (48): $f_{1e} = -2.227$, $f_{2e} = -7.516 \times 10^3$, $f_{3e} - 8.328 \times 10^{-4}$, and $f_{4e} = -9.495 \times 10^{-5}$.

5.2. Simulation Results

In the MATLAB/SIMULINK environment, we conduct simulation experiments on a DG system equipped with a mixed H_2/H_∞ robust integrated controller to verify the effectiveness of the controller described by Equation (49). The simulation parameters relevant to our study are presented in Table 1. During the comparative simulations, we employe specific parameter values for the PID speed controller: $K_p = 16.1313$, $K_i = 13.4692$, and $K_d = 0$. Similarly, the PID excitation controller is configured with the following parameters: $K_p = 50$, $K_i = 10$, and $K_d = 0$. The PID parameters for the speed control section are determined through optimization using the CPSOGSA algorithm, taking into account the desired system performance and stability. On the other hand, the parameters for the excitation control section are chosen based on prior research findings and practical expertise. By employing this combined approach, we aim to achieve an optimal balance between the speed control and excitation control of the DG system. The CPSOGSA optimization process effectively adjusts the PID parameters for the speed control section, ensuring an improved system response and improved system performance. Meanwhile, the predefined values for the excitation control parameters provide a solid foundation based on previous knowledge in the field.

Firstly, the comparison simulation experiment of DG no-load starting characteristics is carried out. When no load is connected, the DG start-up process is controlled by the controller and PID controller proposed in this paper, respectively. The simulation results are shown in Figures 11 and 12. It can be seen from the speed curve diagram in Figure 11 that from 0 to the establishment of the speed of 1 p.u, the proposed controller is about 3 s faster than the PID controller. From the voltage change curve in Figure 12, it can be seen that from 0 to 1 p.u of the machine terminal voltage, our controller is 10 s faster than the PID controller and has better start-up performance. It should be noted that the dead zone of the actuator is not limited in the simulation in this paper. Therefore, the speed of the

DG described in the simulation results reaches the rated value extremely fast under the proposed controller action.

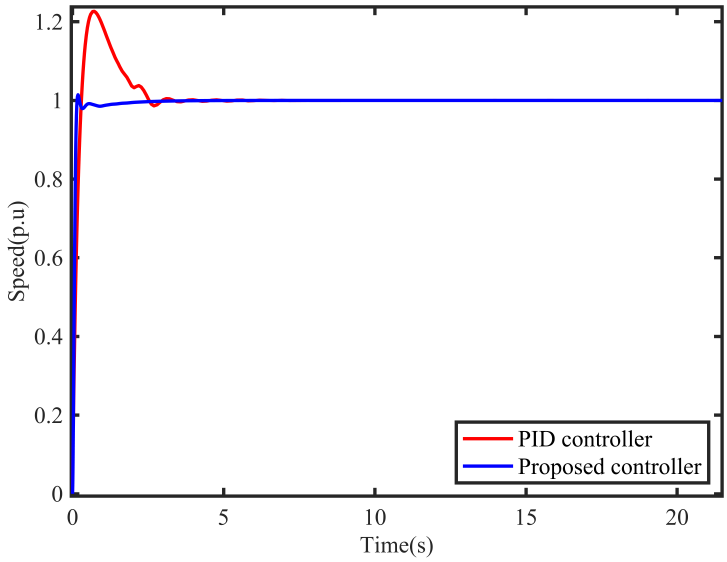

Figure 11. Variation curve of speed at no-load start-up.

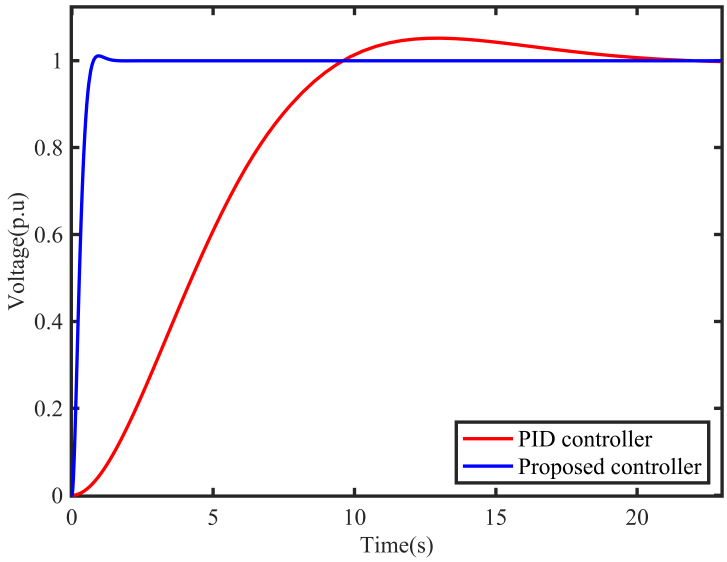

Figure 12. Variation curve of voltage at no-load start-up.

Then, the computer simulation of the designed system with sudden static loads is carried out. Figures 13 and 14 show the dynamic characteristic curves of the speed and voltage of the system after sudden static loads, and the two variables are per unit value. Among them, the blue curve represents the action result of the intelligent nonlinear H_2/H_∞ integrated controller, and the red curve represents the action result of the conventional PID controller.

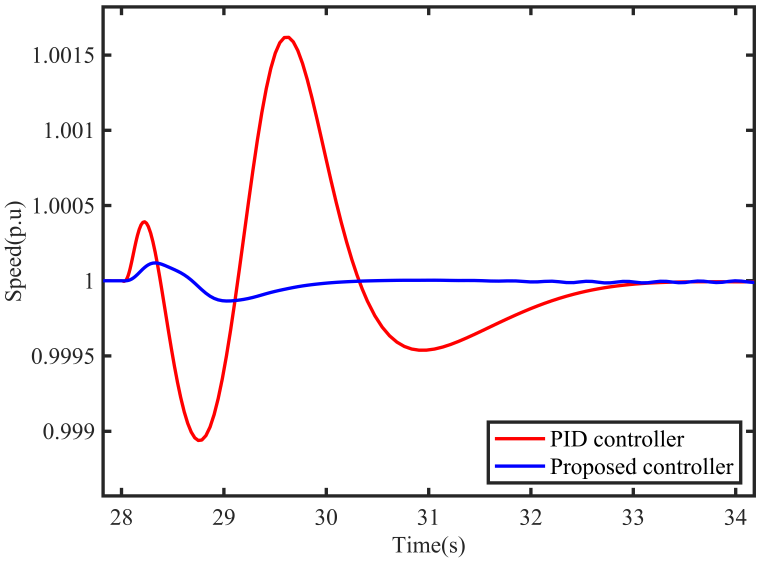

Figure 13. Speed response of system on suddenly increasing static load.

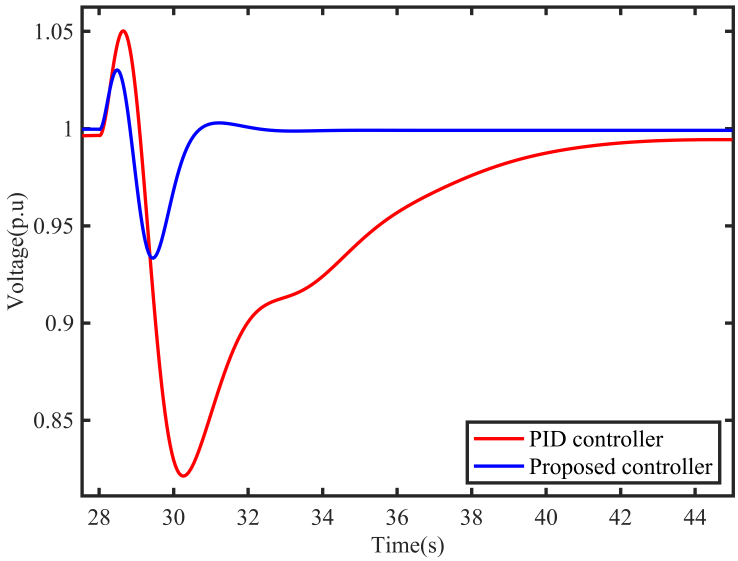

Figure 14. Voltage dynamic response of system on suddenly static load.

From the simulation results, the dynamic performance of the proposed controller is excellent. The dynamic regulation rate is minimal, the stabilization time is about 2 s, the dynamic voltage regulation rate is only about 0.05, and the stabilization time is 4 s. Then, when the conventional PID controller is applied, the dynamic regulation rate of the system is significant, and the stabilization time takes 5 s. The dynamic regulation rate of the system exceeds 0.15, and the stabilization takes a long time. It can be seen through computer simulation that after using the proposed controller, the rate and voltage rate are both decreased, and the stabilization time is shortened.

Finally, a simulation is performed that introduces a simulation of dynamic loads such as PMSM in the system. The dynamic loads greatly influences the grid voltage, especially when the grid is unloaded. The simulation runs for 55 s to connect to a PMSM with a size of 90 kW. The simulation results are shown in Figures 15 and 16. From the situation of the speed change in Figure 15, when the controller proposed in this paper is used, the system shows very little oscillation, while when the PID controller is used, the number of speed oscillations of the system exceeds five times. Figure 16 shows the response process of the

terminal voltage under this working condition, and the controller proposed in this paper also shows better performance.

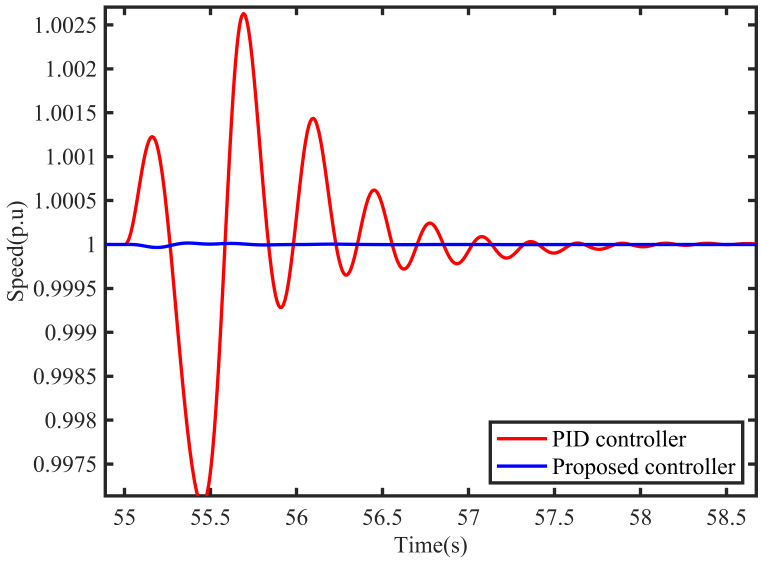

Figure 15. Speed response of system on suddenly increasing dynamic load.

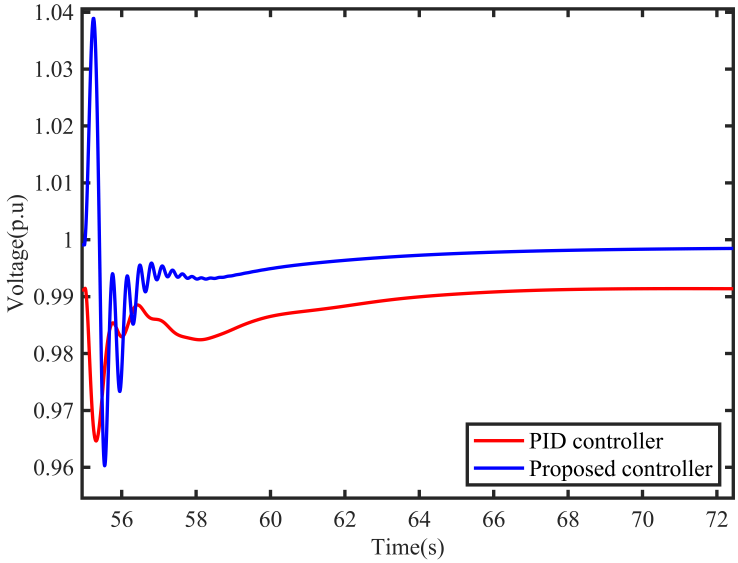

Figure 16. Voltage dynamic response of system on suddenly dynamic load.

In this paper, the intelligent nonlinear integrated controller effectively improves the dynamic accuracy of speed control and excitation control. The improvement of dynamic accuracy weakens the mutual influence and interaction between speed and voltage and solves the comprehensive control problem of speed and voltage. The method improves the stability of the MG system.

6. Conclusions

This paper firstly establishes a nonlinear dynamic model for a diesel generator (DG) and designs speed and excitation controllers for the DG. In the design process, we adopt the direct feedback linearization method and the multi-objective robust control theory. However, there are certain difficulties in determining the weighting parameters. To address this issue, we introduce the artificial intelligence CPSOGSA optimization algorithm to optimize

the relevant weighting parameters that affect the controller performance. To validate the effectiveness of the proposed controller in improving a microgrid (MG) system powered by a DG, we create an MG model driven by a DG in Simulink and conduct corresponding simulation experiments. The simulation results demonstrate that compared to the traditional PID controller, the proposed controller effectively enhances the system's dynamic accuracy and disturbance suppression capability, thereby reducing fluctuations during load transients and operational condition changes. As a result, the stability of the MG system supplied by the DG is significantly improved. In summary, the nonlinear dynamic model and optimized controller proposed in this article exhibit excellent performance in an MG system driven by a DG, exerting positive effects on system stability and response characteristics. These research findings provide valuable references and guidance for the further optimization and enhancement of the application of DGs in MG systems.

Author Contributions: Conceptualization, Y.Z.; methodology, Y.Z. and B.X.; software, B.X.; validation, Y.Z. and B.X.; formal analysis, Y.Z.; investigation, Y.Z.; resources, Z.X.; data curation, Z.X. and J.Q.; writing—original draft preparation, Y.Z. and B.X.; writing—review and editing, Y.Z. and B.X.; visualization, J.Q.; supervision, Z.X.; project administration, Z.X. and J.Q.; and funding acquisition, Z.X. and J.Q. All authors have read and agreed to the published version of the manuscript.

Funding: This research was funded by the National Natural Science Foundation of China (No. 51869007 and 51979204).

Institutional Review Board Statement: Not applicable.

Informed Consent Statement: Not applicable.

Data Availability Statement: Data sharing is not applicable to this article as no datasets were generated or analysed during the current study.

Conflicts of Interest: The authors declare no conflict of interest.

References

1. Muresan, C.I.; Birs, I.; Ionescu, C.; Dulf, E.H.; De Keyser, R. A review of recent developments in autotuning methods for fractional-order controllers. *Fractal Fract.* **2022**, *6*, 37. [CrossRef]
2. Belboul, Z.; Toual, B.; Kouzou, A.; Mokrani, L.; Bensalem, A.; Kennel, R.; Abdelrahem, M. Multiobjective optimization of a hybrid PV/Wind/Battery/Diesel generator system integrated in microgrid: A case study in Djelfa, Algeria. *Energies* **2022**, *15*, 3579. [CrossRef]
3. Amiryar, M.E.; Pullen, K.R. Assessment of the carbon and cost savings of a combined diesel generator, solar photovoltaic, and flywheel energy storage islanded grid system. *Energies* **2019**, *12*, 3356. [CrossRef]
4. Hemeida, A.M.; Omer, A.S.; Bahaa-Eldin, A.M.; Alkhalaf, S.; Ahmed, M.; Senjyu, T.; El-Saady, G. Multi-objective multi-verse optimization of renewable energy sources-based micro-grid system: Real case. *Ain Shams Eng. J.* **2022**, *13*, 101543. [CrossRef]
5. Hasankhani, A.; Hakimi, S.M. Stochastic energy management of smart microgrid with intermittent renewable energy resources in electricity market. *Energy* **2021**, *219*, 119668. [CrossRef]
6. Hakimi, S.M.; Hasankhani, A.; Shafie-khah, M.; Catalão, J.P. Stochastic planning of a multi-microgrid considering integration of renewable energy resources and real-time electricity market. *Appl. Energy* **2021**, *298*, 117215. [CrossRef]
7. Hu, J.; Shan, Y.; Guerrero, J.M.; Ioinovici, A.; Chan, K.W.; Rodriguez, J. Model predictive control of microgrids–An overview. *Renew. Sustain. Energy Rev.* **2021**, *136*, 110422. [CrossRef]
8. Marqusee, J.; Becker, W.; Ericson, S. Resilience and economics of microgrids with PV, battery storage, and networked diesel generators. *Adv. Appl. Energy* **2021**, *3*, 100049. [CrossRef]
9. Bouchekara, H.R.; Javaid, M.S.; Shaaban, Y.A.; Shahriar, M.S.; Ramli, M.A.; Latreche, Y. Decomposition based multiobjective evolutionary algorithm for PV/Wind/Diesel Hybrid Microgrid System design considering load uncertainty. *Energy Rep.* **2021**, *7*, 52–69. [CrossRef]
10. Guo, Y.; Lei, X.; Wang, Q. Capacity coordination planning of isolated microgrid and battery swapping station based on the quantum behavior particle swarm optimization algorithm. *Int. Trans. Electr. Energy Syst.* **2021**, *31*, e12804. [CrossRef]
11. Rameshar, V.; Sharma, G.; Bokoro, P.N.; Çelik, E. Frequency Support Studies of a Diesel–Wind Generation System Using Snake Optimizer-Oriented PID with UC and RFB. *Energies* **2023**, *16*, 3417. [CrossRef]
12. Ahmed, M.; Meegahapola, L.; Vahidnia, A.; Datta, M. Stability and control aspects of microgrid architectures–A comprehensive review. *IEEE Access* **2020**, *8*, 144730–144766. [CrossRef]
13. McGowan, D.J.; Morrow, D.J.; Fox, B. Multiple input governor control for a diesel generating set. *IEEE Trans. Energy Convers.* **2008**, *23*, 851–859. [CrossRef]

14. Zou, Y.; Qian, J.; Zeng, Y.; Ismai, S.; Dao, F.; Feng, Z.; Nie, C.; Mei, H. Optimized Robust Controller Design Based on CPSOGSA Optimization Algorithm and H-two/H-infty Weights Distribution Method for Load Frequency Control of Micro-Grid. *IEEE Access* **2021**, *9*, 162093–162107. [CrossRef]
15. Qian, J.; Guo, Y.; Zou, Y.; Yu, S. Hamiltonian Modeling and Structure Modified Control of Diesel Engine. *Energies* **2021**, *14*, 2011. [CrossRef]
16. Latif, A.; Hussain, S.S.; Das, D.C.; Ustun, T.S. Double stage controller optimization for load frequency stabilization in hybrid wind-ocean wave energy based maritime microgrid system. *Appl. Energy* **2021**, *282*, 116171. [CrossRef]
17. Ali, H.; Magdy, G.; Xu, D. A new optimal robust controller for frequency stability of interconnected hybrid microgrids considering non-inertia sources and uncertainties. *Int. J. Electr. Power Energy Syst.* **2021**, *128*, 106651. [CrossRef]
18. Valenzuela, M.A.; Bentley, J.M.; Lorenz, R.D. Evaluation of torsional oscillations in paper machine sections. *IEEE Trans. Ind. Appl.* **2005**, *41*, 493–501. [CrossRef]
19. Al-Suod MM, S.; Oleksandr, U. Optimization of the Speed Controller in Gas Diesel Device Including in the Autonomous Electric Power System. *WSEAS Trans. Circuits Syst.* **2019**, *18*, 135–140.
20. Iwanski, G.; Bigorajski, Ł.; Koczara, W. Speed control with incremental algorithm of minimum fuel consumption tracking for variable speed diesel generator. *Energy Convers. Manag.* **2018**, *161*, 182–192. [CrossRef]
21. Afzal Thoker, Z.; Ahmad Lone, S. Dynamic performance improvement of wind-diesel power system through robust sliding mode control of hybrid energy storage system. *Wind. Eng.* **2022**, *46*, 1065–1079. [CrossRef]
22. Wang, R.; Li, X.; Ahmed, Q.; Liu, Y.; Ma, X. Speed control of a marine engine using predictive functional control based PID controller. In Proceedings of the 2018 Annual American Control Conference (ACC), Milwaukee, WI, USA, 27–29 June 2018; IEEE: Piscataway, NJ, USA, 2018; pp. 3908–3914.
23. Tran, T.A. The optimization of marine diesel engine rotational speed control process by fuzzy logic control based on particle swarm optimization algorithm. *Future Internet* **2018**, *10*, 99. [CrossRef]
24. Tran, T.A.; Haidara, G. A research on marine diesel engine speed controller by fuzzy logic control theory based on experimental investigation. *World* **2019**, *17*, 19. [CrossRef]
25. Ding, Y.; Shi, W.; Zhang, Y.; Guo, H. Design of Neural Network Speed Controller for Marine Diesel Generator Set. *Int. Core J. Eng.* **2021**, *7*, 586–592.
26. Asgari, S.; Suratgar, A.A.; Kazemi, M.G. Feedforward fractional order PID load frequency control of microgrid using harmony search algorithm. *Iran. J. Sci. Technol. Trans. Electr. Eng.* **2021**, *45*, 1369–1381. [CrossRef]
27. He, Y.; Fan, A.; Wang, Z.; Liu, Y.; Mao, W. Two-phase energy efficiency optimisation for ships using parallel hybrid electric propulsion system. *Ocean Eng.* **2021**, *238*, 109733. [CrossRef]
28. Li, J. *Design and Application of Modern Synchronous Generator Excitation Systems*; John Wiley & Sons: Hoboken, NJ, USA, 2019.
29. Chakraborty, C.; Basak, S.; Rao, Y.T. Synchronous generator with embedded brushless synchronous exciter. *IEEE Trans. Energy Convers.* **2019**, *34*, 1242–1254. [CrossRef]
30. Krishnamurthy, S.; Jahns, T.M.; Lasseter, R.H. The operation of diesel gensets in a CERTS microgrid. In Proceedings of the 2008 IEEE Power and Energy Society General Meeting-Conversion and Delivery of Electrical Energy in the 21st Century, Pittsburgh, PA, USA, 20–24 July 2008; IEEE: Piscataway, NJ, USA, 2008; pp. 1–8.
31. Gayatri, M.T.; Parimi, A.M.; Kumar, A.P. A review of reactive power compensation techniques in microgrids. *Renew. Sustain. Energy Rev.* **2018**, *81*, 1030–1036. [CrossRef]
32. Patel, R.; Hafiz, F.; Swain, A.; Ukil, A. Nonlinear excitation control of diesel generator: A command filter backstepping approach. *IEEE Trans. Ind. Inform.* **2020**, *17*, 4809–4817. [CrossRef]
33. Zhao, P.; Yao, W.; Wen, J.; Jiang, L.; Wang, S.; Cheng, S. Improved synergetic excitation control for transient stability enhancement and voltage regulation of power systems. *Int. J. Electr. Power Energy Syst.* **2015**, *68*, 44–51. [CrossRef]
34. Ramakrishnan, K. Delay-dependent stability of networked generator-excitation control systems: An LMI based approach. *IFAC-PapersOnLine* **2016**, *49*, 431–436. [CrossRef]
35. Berkoune, K.; Sedrine, E.B.; Vido, L.; Le Ballois, S. Robust control of hybrid excitation synchronous generator for wind applications. *Math. Comput. Simul.* **2017**, *131*, 55–75. [CrossRef]
36. Pramanik, M.A.; Roy, T.K.; Ghosh, S.K.; Anower, M.S.; Mahmud, M.A. Robust partial feedback linearizing excitation controller design for higher-order synchronous generator in smib systems to improve the transient stability. In Proceedings of the 2021 IEEE Texas Power and Energy Conference (TPEC), College Station, TX, USA, 2–5 February 2021; IEEE: Piscataway, NJ, USA, 2021; pp. 1–6.
37. Orchi, T.F.; Roy, T.K.; Mahmud, M.A.; Oo, A.M. Feedback linearizing model predictive excitation controller design for multimachine power systems. *IEEE Access* **2017**, *6*, 2310–2319. [CrossRef]
38. Roy, T.K.; Mahmud, M.A.; Shen, W.; Oo, A.M.; Haque, M.E. Robust nonlinear adaptive backstepping excitation controller design for rejecting external disturbances in multimachine power systems. *Int. J. Electr. Power Energy Syst.* **2017**, *84*, 76–86. [CrossRef]
39. Mobarra, M.; Rezkallah, M.; Ilinca, A. Variable speed diesel generators: Performance and characteristic comparison. *Energies* **2022**, *15*, 592. [CrossRef]
40. Mobarra, M.; Tremblay, B.; Rezkallah, M.; Ilinca, A. Advanced control of a compensator motor driving a variable speed diesel generator with rotating stator. *Energies* **2020**, *13*, 2224. [CrossRef]

41. Huang, M.L.; Song, K.M.; Wei, Z.D. Nonlinear H-two/H-infinity synthetic controller for diesel-generator set. *Control Theory Appl.* **2011**, *28*, 885–893.
42. Issa, M.; Ibrahim, H.; Lepage, R.; Ilinca, A. A review and comparison on recent optimization methodologies for diesel engines and diesel power generators. *J. Power Energy Eng.* **2019**, *7*, 31. [CrossRef]
43. Ramstedt, M. Cylinder-by-Cylinder Diesel Engine Modelling: A Torque-Based Approach. Master's Thesis, Linköping University, Department of Electrical Engineering, Linkoping, Sweden, 2004.
44. Zhang, Y.; Zhang, X.; Qian, T.; Hu, R. Modeling and simulation of a passive variable inertia flywheel for diesel generator. *Energy Rep.* **2020**, *6*, 58–68. [CrossRef]
45. Huang, M.; Wang, C. Nonlinear mathematical model of diesel generator sets in marine power stations. *J. Harbin Eng. Univ.* **2006**, *27*, 15–19.
46. Huang, M.L.; Wei, Z.D.; Song, K.M. Synchronous generator state feedback H-infty regulator for marine power plants. *J. Power Syst. Autom.* **2011**, *23*, 15–20.
47. Huang, M.; Wang, C. Simulation study of H-infty governor for diesel engines in marine power stations. *J. Electr. Eng. Technol.* **2006**, *10*, 125–129.
48. Zou, Y.; Hu, W.; Xiao, Z.; Wang, Y.; Chen, J.; Zheng, Y.; Qian, J.; Zeng, Y. Design of intelligent nonlinear robust controller for hydro-turbine governing system based on state-dynamic-measurement hybrid feedback linearization method. *Renew. Energy* 2023, *in press*.
49. Dao, F.; Zou, Y.; Zeng, Y.; Qian, J.; Li, X. An intelligent CPSOGSA-based mixed H-two/H-infty robust controller for the multi-hydro-turbine governing system with sharing common penstock. *Renew. Energy* 2023, *in press*.
50. Li, L.; Qian, J.; Zou, Y.; Tian, D.; Zeng, Y.; Cao, F.; Li, X. Optimized Takagi–Sugeno Fuzzy Mixed H-two/H-infty Robust Controller Design Based on CPSOGSA Optimization Algorithm for Hydraulic Turbine Governing System. *Energies* **2022**, *15*, 4771. [CrossRef]
51. Duman, S.; Li, J.; Wu, L.; Guvenc, U. Optimal power flow with stochastic wind power and FACTS devices: A modified hybrid PSOGSA with chaotic maps approach. *Neural Comput. Appl.* **2020**, *32*, 8463–8492. [CrossRef]
52. Rather, S.A.; Bala, P.S. Constriction coefficient based particle swarm optimization and gravitational search algorithm for multilevel image thresholding. *Expert Syst.* **2021**, *38*, e12717. [CrossRef]
53. Rather, S.A.; Bala, P.S. A hybrid constriction coefficient-based particle swarm optimization and gravitational search algorithm for training multi-layer perceptron. *Int. J. Intell. Comput. Cybern.* **2020**, *13*, 129–165. [CrossRef]
54. Xie, S.; Zeng, Y.; Qian, J.; Yang, F.; Li, Y. CPSOGSA Optimization Algorithm Driven Cascaded 3DOF-FOPID-FOPI Controller for Load Frequency Control of DFIG-Containing Interconnected Power System. *Energies* **2023**, *16*, 1364. [CrossRef]
55. Rather, S.A.; Bala, P.S. Hybridization of constriction coefficient-based particle swarm optimization and chaotic gravitational search algorithm for solving engineering design problems. In *Applied Soft Computing and Communication Networks: Proceedings of ACN 2019*; Springer: Singapore, 2020; pp. 95–115.